Bioactive Materials 20 (2023) 610–626

Contents lists available at ScienceDirect

Bioactive Materials

journal homepage: www.keaipublishing.com/en/journals/bioactive-materials

A novel sprayable thermosensitive hydrogel coupled with zinc modified metformin promotes the healing of skin wound

Zhengwei Liu [a,1], Wanze Tang [a,1], Jiayi Liu [c,1], Yingying Han [a], Qinnan Yan [a], Yuechao Dong [a], Xiaomei Liu [b], Dazhi Yang [d], Guixing Ma [a,**], Huiling Cao [a,*]

[a] Department of Biochemistry, School of Medicine, Southern University of Science and Technology, Guangdong Provincial Key Laboratory of Cell Microenvironment and Disease Research, Shenzhen Key Laboratory of Cell Microenvironment, Shenzhen, 518055, China
[b] Southern University of Science and Technology, Shenzhen, 518055, China
[c] Department of Biomedical Engineering, Southern University of Science and Technology, Shenzhen, 518055, China
[d] The First Affiliated Hospital, Southern University of Science and Technology, Shenzhen, 518055, China

ARTICLE INFO

Keywords:
Thermosensitive hydrogel
Skin wound
ZnMet-PF127
Reactive oxygen species (ROS)
Autophagy

ABSTRACT

A novel sprayable adhesive is established (ZnMet-PF127) by the combination of a thermosensitive hydrogel (Pluronic F127, PF127) and a coordination complex of zinc and metformin (ZnMet). Here we demonstrate that ZnMet-PF127 potently promotes the healing of traumatic skin defect and burn skin injury by promoting cell proliferation, angiogenesis, collagen formation. Furthermore, we find that ZnMet could inhibit reactive oxygen species (ROS) production through activation of autophagy, thereby protecting cell from oxidative stress induced damage and promoting healing of skin wound. ZnMet complex exerts better effects on promoting skin wound healing than $ZnCl_2$ or metformin alone. ZnMet complex also displays excellent antibacterial activity against *Staphylococcus aureus* or *Escherichia coli,* which could reduce the incidence of skin wound infections. Collectively, we demonstrate that sprayable PF127 could be used as a new drug delivery system for treatment of skin injury. The advantages of this sprayable system are obvious: (1) It is convenient to use; (2) The hydrogel can cover irregular skin defect sites evenly in a liquid state. In combination with this system, we establish a novel sprayable adhesive (ZnMet-PF127) and demonstrate that it is a potential clinical treatment for traumatic skin defect and burn skin injury.

1. Introduction

Skin injury is the destruction of the physiological structure and function, which manifests as a local impairment of skin tissue. The skin tissue exhibits restricted self-repair ability. For certain types of skin wound, such as deep skin wounds, skin burns and diabetic ulcers, it is difficult to heal thoroughly by self-repair ability of skin. The heal of these severe skin wounds often require surgery (such as skin grafting) or skin reconstruction by using bioactive dressing materials [1].

Skin wound healing is a multi-step process, consists of inflammatory, proliferative, and mature periods. Wound inflammation in the early period is characterized by the recruitment of neutrophils and macrophages to the trauma area, under the chemotaxis of inflammatory factors such as IL-1β, IL-6, TNF-α, etc. Angiogenesis play an important role in the mature of wound tissue [2]. The proliferative phase, also called the granulation tissue phase, follows the inflammatory phase. During this phase, the formation of new capillaries and proliferation of fibroblasts greatly promote granulation tissue formation [3,4]. The mature phase, also known as the remodeling phase, occurs 2–3 weeks after injury. Fibroblasts secrete extracellular matrix such as collagen fibers, and then the irregular collagen fiber is gradually replaced by newly synthesized collagen fiber, which is more regular and elastic [5,6]. Excessive reactive oxygen species (ROS) accumulation and inflammation delays wound healing and even aggravates wound injury [7].

Metformin, a biguanide, is currently the first-line drug for the initial treatment of type 2 diabetes (T2D) because of its inhibitory effect on

Peer review under responsibility of KeAi Communications Co., Ltd.
* Corresponding author. Southern University of Science and Technology, 1088 Xueyuan Rd, Shenzhen, 518055, China.
** Corresponding author. Southern University of Science and Technology, 1088 Xueyuan Rd, Shenzhen, 518055, China.
E-mail addresses: magx@mail.sustech.edu.cn (G. Ma), caohl@sustech.edu.cn (H. Cao).
[1] These authors contributed equally to this study.

https://doi.org/10.1016/j.bioactmat.2022.06.008
Received 15 May 2022; Received in revised form 13 June 2022; Accepted 14 June 2022

liver glucose production [8–10]. Metformin also shows significant anti-inflammatory effects which has been demonstrated by abundant fundamental research and clinical trials [11,12]. Several clinical studies showed that oral metformin administration has modest anti-systemic inflammation effect [13,14]. It has also been reported that metformin can reduce pro-inflammatory cytokines (IL-1β, TNF-α) and macrophage migration inhibitor (MIF) in vivo [15]. In addition, metformin reduces the production of ROS during diabetic nephropathy [16]. In addition, positive effects of metformin on various inflammatory skin diseases (psoriasis, acanthosis nigricans, acne, etc.) have also been reported [17]. However, as for skin wound healing, while some researchers suggest a positive role of metformin, a negative role of metformin for skin wound healing by inhibition of human keratinocyte proliferation is also reported [18,19].

Zinc (Zn), an essential trace element in human bodies, exerts key roles on human growth, development, immunity response, etc. [20]. Zinc exists in many enzyme systems, such as carbonic anhydrase, protein kinase, respiratory enzyme, lactate dehydrogenase, superoxide dismutase, alkaline phosphatase, DNA and RNA polymerase, etc. [21,22]. Metabolic activation of these enzymes requires zinc ions, which plays important roles in the process of wound repair [23]. Clinically, zinc sulfate has been widely used in wound care of patients with decubital ulcers [24]. Zinc ion also plays important roles in promoting skin wound healing due to its prominent roles in antibacterial, promoting fibroblast proliferation, accelerating ECM synthesis and secretion, and reducing the production of free radicals to ensure cellular viability [25].

Based on the reported functions of both metformin and zinc, we hypothesized that zinc modified metformin (ZnMet) may have potent effect on promoting skin wound healing. ZnMet is a coordination complex that has a stoichiometric ratio of 1:2 (Zn: metformin) [26]. We equip ZnMet with biocompatibility, anti-inflammatory, antioxidant and antibacterial properties by the principle of complexation between zinc ion and metformin. Hydrogels are widely used as drug delivery systems in tissue engineering and damage repair, and the application of sprayable hydrogels in the repair of skin injuries is receiving more and more attention [27,28]. In this study, by using Pluronic F127 (PF127, also known as Poloxamer 407), a temperature sensitive hydrogel which is liquid at low temperatures and gradually transforms into a semisolid gel form when temperature arises [29], we synthesize a novel sprayable adhesive (ZnMet-PF127) for treatment of skin wound and skin burns. Sprayable ZnMet-PF127 can cover the surface of irregular skin defect evenly in the form of liquid below room temperature. It is worth noting that we for the first time apply thermosensitive hydrogel PF127 as a spray for skin wound healing by taking advantage of its reversible thermal response. Liquid PF127 is applied to the wound by a nebulizer and solidifies into a semi-solid state once it contacts the skin surface. It is convenient to use. Through in vivo and in vitro experiments, we demonstrate that ZnMet-PF127 greatly accelerates skin wound healing in mouse models with traumatic skin defects and skin burns. Mechanistically, we find that ZnMet-PF127 dramatically promotes angiogenesis, cell proliferation, granulation tissue formation, collagen deposition. Furthermore, we find that ZnMet could inhibit ROS production through activation of autophagy, thereby inhibiting inflammation, protecting cell from oxidative stress induced damage and promoting healing of skin wound. Thus, we demonstrate that ZnMet-PF127 is a potential clinical treatment for traumatic skin defect and skin burns.

2. Materials and Methods

2.1. Synthesis of ZnMet-Pluronic F127

A schematic diagram of preparation process and application was shown in Fig. 1. Metformin hydrochloride (MW = 165.62 Da) and zinc chloride hexahydrate were obtained from Macklin company. Pluronic F127 was from Aladdin company. All materials and reagents were not further purified unless otherwise stated. Deionized (DI) water (>18.2 MΩ cm) was used in this study.

Synthesis of ZnMet complex: Guanidine hydrochloride and zinc chloride hexahydrate were dissolved in anhydrous alcohol at a concentration ratio of 2:1, then metformin hydrochloride solution was added slowly into zinc chloride solution. The whole reaction system was maintained at 50 °C for full reaction with continuous magnetic stirring for 6 h until the micro crystal was precipitated. The crystal product was collected, washed repeatedly with a small amount of ethanol, and vacuum filtrated through Bouchard funnel. Finally, the products were lyophilized [26]. The content of zinc irons in ZnMet was indirectly calculated by the elemental analyzer. The concentration and the ratio of zinc in ZnMet complex were analyzed by inductively coupled plasma mass spectrometry (ICP-MS) (Agilent 7700X) (Table 2).

Preparation of ZnMet-Pluronic F127: Pluronic F127 powder was stirred overnight in normal saline to make 5%, 10%, 16%, 20% and 25% solutions at 4 °C. Then ZnMet was added into the above Pluronic F127 solutions to form a final concentration of ZnMet at 50 μM [30].

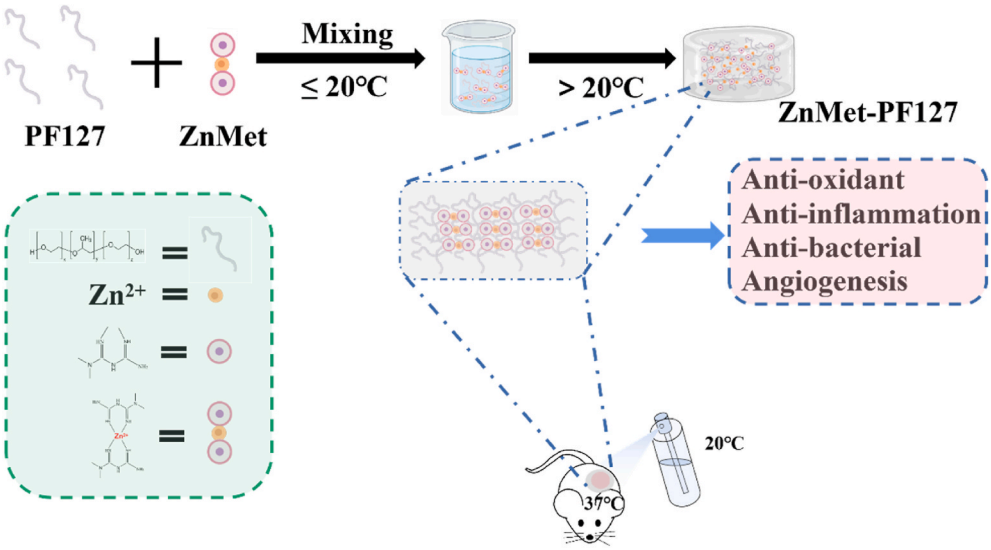

Fig. 1. Schematic diagram of ZnMet-PF127 preparation process and application.

Table 1
Primers used for RT-qPCR.

Gene name	Sequences (5′-3′)
IL-6	F: CTGCAAGAGACTTCCATCCAG
	R: AGTGGTATAGACAGGTCTGTTGG
TNF-α	F: CCCTCACACTCAGATCATCTTCT
	R: GCTACGACGTGGGCTACAG
IL-1β	F: GCAACTGTTCCTGAACTCAACT
	R: ATCTTTTGGGGTCCGTCAACT
iNOS	F: TGTCTGCAGCACTTGGATCAGGAA
	R: GAAGCCACTGACACTTCGCACAAA
VEGF	F: TGGTGGACATCTTCCAGGAGTA
	R: GCACACAGGACGGCTTGAA
GAPDH	F: AGAAGGCTGGGGCTCATTT
	R: CTGGAAGGTGGACAGCGAGG

3. Examination of ZnMet properties

The attenuated total reflection (ATR) patterns of metformin (Met) and ZnMet were characterized by Fourier Transform Infrared Spectroscopy (FTIR Spectroscopy) (PerkinElmer, Frontier) with a wavenumber from 500 to 4000 cm^{-1} at room temperature. The thermal properties of the samples were evaluated by thermogravimetric analyzer (TGA) (Gas Analyzer, TGA55). TGA data were recorded for each analyzed sample in the temperature range of 50–800 °C. ^{1}H NMR (nuclear magnetic resonance) and ^{13}C NMR analyses of Met and ZnMet were performed using nuclear magnetic resonance spectroscopy (Bruker, AVANCE III 500 MHz) and n2-cryoo-platform for Prodigy probe. Samples were dissolved with d6-DMSO solvent. The experimental procedure was carried out at room temperature [31]. Data acquisition was performed with Bruker's TopSpin 3.2 software and processed with MestReNova 14.1 (Mestrelab Research S.L.). The stability of ZnMet was tested by high-performance liquid chromatography (HPLC) (Agilent 1260 Infinity) with a diode array detector for the content and purity of ZnMet aqueous solution at day 0 and 14. Column type is EclipsePlus C18. Mobile phase: potassium dihydrogen phosphate solution (0.01 M, pH 3.5): acetonitrile = 75:35 [32].

Characterization of Pluronic F127 hydrogel: The fluid morphology of PF127 thermosensitive hydrogel was examined at room temperature and 37 °C, respectively. The ability of ZnMet-PF127 to fill in irregular skin defects evenly in a liquid state was also examined. We introduced irregular shapes to agarose gel and found that ZnMet-PF127 could perfectly fit into those irregular shapes (Fig. 2A). The microstructural morphology of Pluronic F127 hydrogel and ZnMet-PF127 were examined by scanning electron microscope (SEM) (Zeiss, Merlin). Surface morphologies were obtained under 5 kV accelerated voltage [33]. All samples were coated with platinum before scanning to improve electrical conductivity. Rheological properties of ZnMet-PF127 hydrogel and PF127 hydrogel were measured using a rotary rheometer (ThermoFisher Scientific, HAAKE MARS 40) [34]. The morphologies of the ZnMet-PF127 samples were examined by transmission electron microscopy (TEM). About 3 μL of sample was gently placed on carbon-coated copper grids (TED Pella, Redding). The grids were discharged before use with a negative current of 15 mA for 10 s. Specimens were prepared in a controlled environment and were allowed to dry at room temperature overnight. Finally, specimens were transferred to a transmission electron microscope (Hitachi, HT7700). Samples were analyzed under low dose conditions with a defocus range of 2–4 μm. Images were taken by an F-416 CMOS camera and EMMENU version 4.0.9.52 (Tvips) software [35].

3.1. In vitro drug release assay

10 mL ZnMet-PF127 was placed in 30 mL of PBS (pH 7.4, pH 4.0, pH 8.9), at 37 °C, with continuous stirring at 100 rpm. At certain time intervals, 1 mL of above solution was taken out and 1 mL of PBS was added into the above solution to maintain a constant volume [36]. The concentration of ZnMet in the solution was analyzed by inductively coupled plasma mass spectrometry (ICP-MS) (Agilent 7700X) to determine the release rate.

3.2. Cell proliferation

Dulbecco's Modified Eagle Medium (DMEM, HyClone) with 10% fetal bovine serum (FBS, Gibco) and 50 U/ml penicillin G plus 50 μg/ml streptomycin sulfate (HyClone) was used for the culture of human embryonic fibroblasts (NIH3T3) and human umbilical vein endothelial cells (HUVEC). The third to fifth generations of NIH3T3 and HUVEC were used. Cells were seeded in 96-well plates at a density of 2×10^3 cells/well and cultured in an incubator at 37 °C with 5% carbon dioxide. After 24 h, cells were treated with different concentrations of drugs (100 μM Met, 50 μM $ZnCl_2$ and 5 μM, 25 μM, 50 μM, 100 μM, 200 μM and 500 μM ZnMet), and cell proliferation was examined by using CCK8 kit (Beyotime, C0038) at day 1, 3 and 5, respectively [37].

3.3. Antibacterial property test

Staphylococcus aureus (*S. aureus*) ATCC6538 and *Escherichia coli (E. coli*) DH5α Strain (Guangzhou Qiyun Biotechnology Co., LTD) were used to evaluate the antibacterial activity. 4 mL *S. aureus and E. coli* suspension (1×10^4 CFUs/mL) were incubated respectively at 37 °C and 170 rpm for 12 h, then 0.5 mL of the above suspension was diluted using broth medium to a concentration of 10^2 CFU/mL and incubated under the above condition for another 12 h. Finally, 20 μL of the above bacterial suspension was applied to an agarose Petri dish and cultured overnight at 37 °C. Colony forming unit (CFU) was counted for each sample [38].

3.4. Quantitative real-time qPCR (RT-qPCR)

Total RNA was isolated using RNAiso Plus (TAKARA, 9108) according to the manufacturer's instruction. Reverse transcription was performed using a reverse transcription kit (Beyotime, D7168 M) from 0.5 μg total RNA according to the manufacturer's instructions [39]. RT-qPCR analyses were performed as we previously described [40]. All samples were normalized to *GAPDH* expression. The DNA sequences of primers used for RT-qPCR analyses in this study are summarized in Table 1.

3.5. Monodansylcadaverine (MDC) staining for autophagosomes

Dulbecco's Modified Eagle Medium (DMEM, HyClone) with 10% fetal bovine serum (FBS, Gibco) and 50 U/ml penicillin G plus 50 μg/ml streptomycin sulfate (HyClone) was used for the culture of human embryonic fibroblasts (NIH3T3). The third to fifth generations of NIH3T3

Table 2
Zn^{2+}/Met ratio in ZnMet determined by ICP-MS.

	ZnMet Weight (mg)	ZnMet Volume (L)	Zn^{2+} Conc. (ppb)	Zn^{2+} Conc. RSD	Zn^{2+} Mass (mg)	Zn^{2+}/Met (mg/mg)	Zn^{2+}/Met (mM/mM)
repeat-1	**10.4**	**5**	**451.072**	**1.303**	**2.26**	**0.278**	**0.549**
repeat-2	**10.4**	**5**	**445.203**	**2.087**	**2.23**	**0.273**	**0.539**
repeat-3	**10.4**	**5**	**445.207**	**0.621**	**2.23**	**0.273**	**0.539**

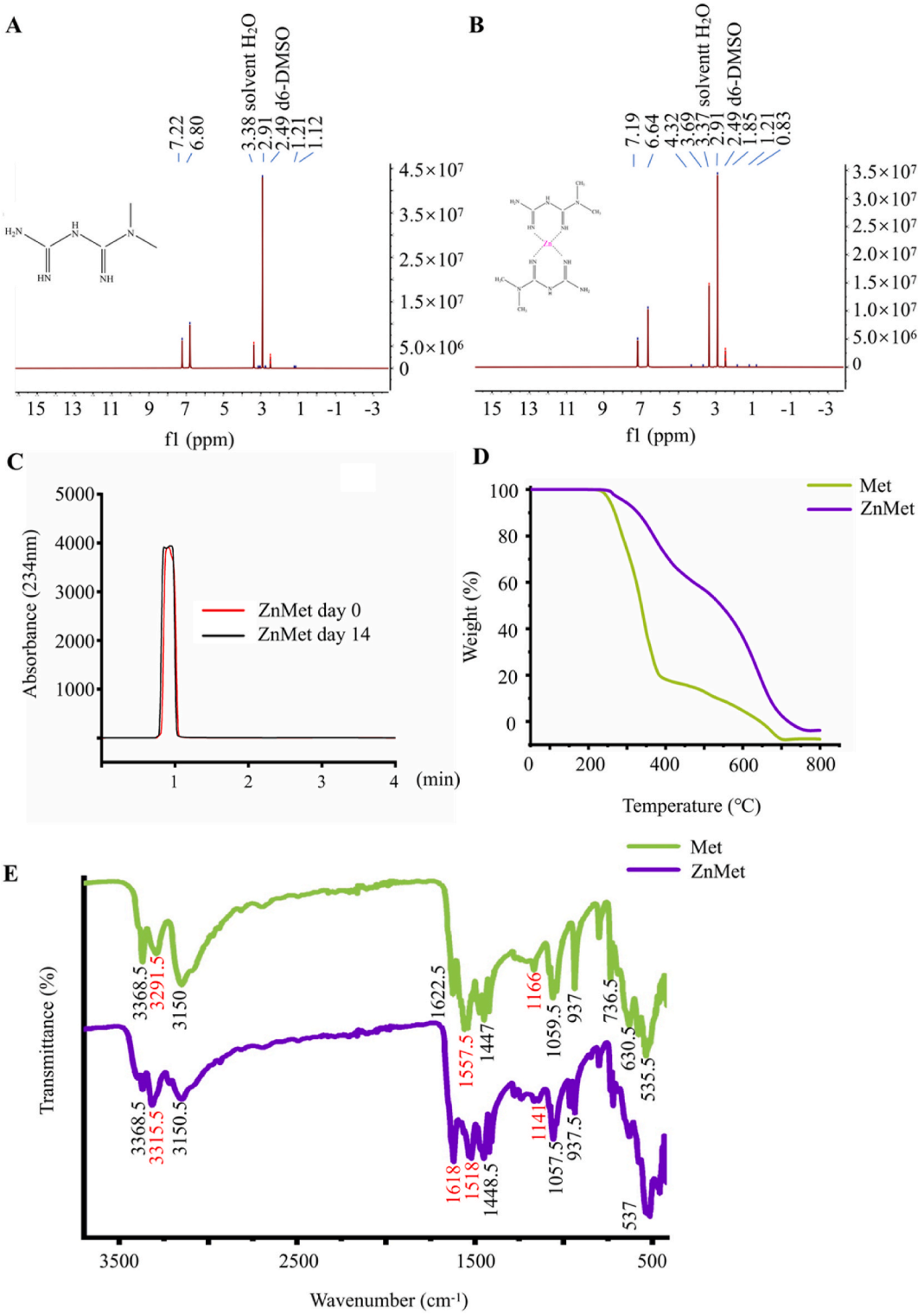

Fig. 2. Characterization of ZnMet.

were used. Cells were seeded in 6-well plates at a density of 1 × 10^6 cells/mL and cultured in an incubator at 37 °C with 5% carbon dioxide. After 24 h, cells were treated with Met (100 μM), $ZnCl_2$ (50 μM) and ZnMet (50 μM), followed by staining with monodansylcadaverine (MDC) for autophagosome (Beyotime; C3018S) at 37 °C for 30 min. After 3 washes with Assay Buffer, the cells were immediately observed under a fluorescence microscope (Nikon confocal A1R with FLIM).

3.6. Determination of reactive oxygen species (ROS)

Reactive oxygen species (ROS) was measured by ROS Assay Kit (Beyotime, S0033S) as previously described with some modification [41]. Briefly, NIH3T3 were incubated with 6-Carboxy-2′, 7′-dichlorodihydrofluorescein diacetate (DCFH-DA) at a final concentration of 10 mM for 20 min and washed 3 times with cell culture medium without FBS. ROS production in NIH3T3 was measured fluorometrically with

excitation and emission settings at 488 nm and 525 nm, respectively.

3.7. Western blot analysis

Western blotting was then performed as previously reported [42–44]. In short, cells were lysed with lysate (Beyotime, P0013). Protein extracts were then separated on a 10% sodium dodecyl sulfate-polyacrylamide gel electrophoresis using a semi-dry apparatus and transferred to a polyvinylidene fluoride (PVDF) membrane (Biorad, USA). Then non-specific sites on the membrane were blocked at room temperature with blocking solution (Beyotime, P0252) for 1 h. After that, the blot was incubated with primary antibody followed by incubation with secondary antibodies conjugated with horseradish peroxidase; and at last, the membrane was visualized using a Western Blotting Detection Kit (Mei5bio, MF-078-01) by chemiluminescence imaging system (LAS4000, ImageQuant). Antibodies were used after a thousand-fold dilution in this project: (GAPDH: ORIGENE, TA-08; LC3B: ABclonal, A19665; P62: ABclonal, A19700; AMPK: HUABIO, ET1608-40; p-AMPK: HUABIO, ET1701-37; VEGF: ABclonal, A12303).

3.8. Animal studies

All mice used in this study were group-housed under the temperature between 20 °C and 24 °C and exposed to a 12-h light/12-h dark cycle. Male C57BL/6 mice weighing 25–30 g were used. Two full-thickness round-shape wounds with a diameter of 8 mm were made on the back of each mouse [45–48]. The modeling process is described below: after anesthetized by inhalation of isoflurane, the mice were placed in the prone position. Hair on the back of the mice was removed with electric scissors, and two full-thickness wounds were made on the back on either side of the midline with an 8 mm biopsy trocar through two layers of skin. After surgery, the mice were kept as one mouse per cage to avoid eaten of the PF127. Mice were randomly divided into the following groups: PF127 (control group), $ZnCl_2$ (50 μM)-PF127, Met (100 μM)-PF127 and ZnMet (50 μM)-PF127, 6 mice for each group (n = 6). Mice were administered every 24 h by spraying using a nebulizer. Wound surface was photographed at day 0, 1, 3, 5, 7 and 9 after surgery. Depending on the healing of the skin wound, all mice were sacrificed at day 11. We also tested if ZnMet-PF127 could promote healing of burn skin injury. Burn skin injury model was established as previously reported [49,50]. After anesthetized with isoflurane, the hair on the back was removed with depilatory cream, and the back was sterilized with iodophor, then a solid aluminum rod (10 mm in diameter, 51 g), which was heated to 100 °C by leaving in boiling water for 10 min, was placed on the back of the mice for 15 s [51]. The wounds were photographed at day 0, 3, 5, 9, 13 and 17 after operation, and depending on the healing of the wound, all mice were sacrificed on day 17 after operation. The protocols for animal study in this project were approved by the Institutional Animal Care and Use Committee of Southern University of Science and Technology (Approval No. SUSTech-JY202112032). In this study, we have complied with all relevant ethical regulations for animal experiments. In order to study the biosafety of ZnMet at specific concentrations in vivo, we examined the pathological changes of heart, liver, spleen, lung and kidney of mice by H&E staining.

3.9. Histomorphological analysis

Hematoxylin and eosin staining (H&E) (Baso, BA4025) was used for histomorphological evaluation of wound regeneration to assess inflammation and epidermal regeneration in the defect area. H&E staining was performed as we previously described [40,52]. After removed from the wound, the skin tissue was fixed with 4% paraformaldehyde immediately for 48 h, then dehydrated with graded alcohol, and finally embedded in paraffin. The skin tissue was sectioned into 5 μm slices, followed by H&E staining for microscopic examination. Briefly, the slices were dewaxed with 100% xylene for 3 min, with 50:50 xylene/100% ethanol for another 3 min, then rehydrated with 100% ethanol for 3 min, with 95% ethanol for another 3min, then stained with hematoxylin (Gill's IX) at room temperature for 5 min, and then washed with deionized water for 5 min. After that, the slices were soaked in acid alcohol (1% HCl in 70% ethanol) for 5 times and rinsed with deionized water. After treated with ammonia (1 ml pure NH_4OH in 1 L water) and rinsed with deionized water, sections were stained with Eosin solution at room temperature for 1 min, and then dehydrated with graded alcohol (95% ethanol for 2 min; 100% ether for 2 min) and cleared by xylene (100% xylene for 30 min). All sections were observed and photographed with optical microscope.

3.10. Masson trichrome staining

The collagen amount was evaluated by Masson trichrome staining (Solarbio, G1340) as we previously described [52]. After deparaffinized and rehydrated, skin tissue samples (5 μm), were treated with Bouin's solution at 56 °C for 15 min. After cooling in a water-bath at 18–26 °C for 5 min, samples were stained using working Weigert's iron hematoxylin solution for 5 min at room temperature. Then, slides were rinsed with deionized water and stained with Biebrich scarlet-acid fuchsin for 5 min at room temperature and rinsed with deionized water for 1 min. Slides were then treated with working phosphotungstic/phosphomolybdic acid solution for 5 min at room temperature and placed in Aniline Blue solution for 5 min at room temperature. Slides were treated with acetic acid (1%) for 2 min at room temperature and dehydrated through a graded alcohol series (70, 80, 90 and 100%), cleared in xylene for 5 min. All sections were photographed using a 400 × light microscope. The collagen volume fraction was analyzed using Fiji-ImageJ software. The relative percentage of collagen density was then calculated using the following equation:

$$\text{Collagen (\%)} = \text{collagen area / total area of skin} \times 100\%$$

3.11. Histological, immunohistochemistry, immunofluorescence examinations

Histological and immunohistochemistry analysis were performed to evaluate the formation of vessels and the number of immune cells during skin wound healing. Immunohistochemistry staining of CD31 (Abcam, ab28364) was used to assess the formation of vessels [53]. F4/80 (Cell Signaling Technology, 70076) was used to assess the number of infiltrated macrophages. TNF-α (Cell Signaling Technology, 11948T) was used to assess the inflammatory state of the skin wound. Slides were subjected to sodium citrate buffer (pH 6.0) at 58 °C for 16 h for antigen retrieval and then incubated with rabbit anti-CD31, F4/80 and TNF-α antibodies, respectively. CD31 positive blood vessel number within unit area was analyzed using Fiji-ImageJ software. The mean signal intensity of F4/80 and TNF-α was analyzed using Fiji-ImageJ software.

3.12. Collagen analysis by two-photon laser microscope

Collagen fibers and second harmonic generation was detected by two-Photon laser microscope (Olympus FVMPE-RS). Two-photon emitted fluorescence signal was collected from each specimen, and the mean signal intensity was analyzed using Fiji-ImageJ software [54,55].

3.13. Statistical analysis

The sample size for each experiment was determined according to our previous experiences. The data were expressed as mean ± standard deviation (SD), as indicated in the figure legends. Student's *t*-test and one-way analysis of variance (ANOVA) were used in this study. Differences with $P < 0.05$ were considered statistically significant.

4. Results and discussion

4.1. Structure, composition, and characteristics of ZnMet

ZnMet complex was obtained by the complexation of $ZnCl_2$ and Met, and the ratio of Zn^{2+} to Met in ZnMet was 1:2 detected by ICP-MS, indicating the successful synthesis of ZnMet (Table 2), which is consistent as previously reported [26].

The ^{1}H NMR spectra of Met and ZnMet were shown in Fig. 2A and B. In the ^{1}H NMR spectrum, proton resonances were all detected at -3-15 ppm. As shown in Table 3, Met free ligand showed the following δ (ppm): 2.91 (6H(A), $2CH_3$ groups), 1.12 (1H, –NH + 2H, $–NH_2$(C), primary and secondary amine), 6.80 and 7.22 (2H(B), both = NH imine groups). ZnMet complex displayed the following δ (ppm): 2.91 (6H(A), $2CH_3$ groups), 0.83 (1H, –NH + 2H, $–NH_2$(C), primary and secondary amine), 6.64 and 7.19 (2H(B), both = NH imine groups [56,57]. These results showed that in the case of ZnMet complex, the signal of 2H(B) was shifted in comparison with the Met, where it can be ascribed to the participation in the chelating process.

The ^{13}C NMR spectral of ZnMet coincided well with the spectral characteristics of Met (Fig. S1). HPLC results were shown in Fig. 2C, the red curve represented the ZnMet HPLC results at day 0 and the black curve represented the HPLC results at day 14. It clearly displayed that the curve peaks at days 0 and 14 overlapped perfectly. The retention time of ZnMet was 0.92 min and 0.94 min, respectively. No interference peak was observed during the retention time of Met. These results indicated that ZnMet had a high purity and excellent stability. TGA results indicated that marked weight loss of Met at the temperature between 250–400 °C may be due to the onset of thermal decomposition. ZnMet also started to lose weight at 250 °C but at a lower speed compared with Met (Fig. 2D). The lower thermal decomposition speed of ZnMet than Met suggested that the thermal stability of Met was greatly elevated by the complexation of Zn ions. FTIR Spectroscopy results of Met and ZnMet revealed the different NH absorption peaks, at the range of 3500–3200 cm^{-1}, between ZnMet and Met reflected the potential involvement of NH in the complexation of Met and Zn ions. (Fig. 2E). And the stretching vibrations of the NH bond was between 1650 and 1550 cm^{-1}. The results indicated that with the gradual generation of ZnMet, NH Peak moved towards 1618 cm^{-1} in ZnMet from 1622.5 cm^{-1} in Met. Moreover, another peak at 1557.5 cm^{-1} in Met also moved to 1518 cm^{-1} which further indicated that the formation of ZnMet complex.

(**A-B**) ^{1}H NMR map of Met (**A**) and ZnMet (**B**). (**C**) HPLC of ZnMet after for 14 days' storage. (**D**) TGA image of Met and ZnMet. Red font indicates the shift of NH–Zn energy. (**E**) FT-IR spectra of Met and ZnMet.

PF127, a temperature sensitive hydrogel which is liquid at low temperatures and gradually transforms into a semisolid gel form when temperature arises. Fig. 3A clearly demonstrated that 20% PF-127 hydrogel can be switched from liquid at room temperature to solid at 37 °C, indicating excellent temperature-sensitivity of PF127 hydrogel. 20% PF127 hydrogel could be adequately filled to irregular defects on agarose gel medium (Fig. 3A). The elastic modulus of ZnMet-PF127 hydrogel depends on concentrations and temperature. The gelation temperature and elastic modulus of ZnMet-PF127 hydrogel and PF127 hydrogel were tested with different concentrations from 10% to 25%. The initial gelation temperature of 20% ZnMet-PF127 hydrogel was around 20 °C (Fig. 3B–E). As showed in Fig. S3, the gelation temperature and elastic modulus of ZnMet-PF127 hydrogel and PF127 hydrogel are similar. This means that ZnMet does not change the properties of PF127 hydrogel. Considering the spraying method of administration, we chose the 20% concentration of ZnMet-PF127 hydrogel for the follow-up experiments, which is also a widely used concentration by other researchers [58–63]. Considering the pH value of the wound surface could affect the healing process, we tested the drug release rate of ZnMet from ZnMet-PF127 under different pH conditions (pH 7.4; pH 4.0; pH 8.9) [64]. Fig. 3F displayed when left in normal physiological environment (PBS, pH = 7.4) for 2 h, the release amount of ZnMet from ZnMet-PF127 hydrogel reached about 40%. When left in an acidic or an alkaline environment (PBS, pH = 4.0 or pH = 8.9) for 2 h, the release amount of ZnMet from ZnMet-PF127 hydrogel reached about 50% and 46% respectively. Therefore, during the first 2 h, the release rate of the drug is high. After 10 h, the drug release amount reached about 100% in acidic or alkaline environments (PBS, pH = 4.0 or pH = 8.9). At the time point of 12 h, the drug release amount reached about 95% in normal physiological environment (PBS, pH = 7.4). This means that the drug release rate of ZnMet-PF127 hydrogel is slightly increased in acidic or alkaline environments. These results suggest that the drug retention ability of PF127 hydrogel is not obvious [65]. The TEM images of the ZnMet-PF127 and PF127 sample (without dyeing) were shown in Fig. 3G. Compared with PF-127 hydrogel, metal-like particles with a diameter of about 10–20 nm were detected in ZnMet-PF127, but not in PF-127, indicating that ZnMet was successfully loaded into PF-127 hydrogel. Negative staining of PF-127 and ZnMet-PF127 (Fig. S2) showed no significant difference, indicating that the loading of ZnMet didn't change the basic structure of PF-127. Similar morphology of PF127 and ZnMet-PF127 were observed by SEM as shown in Fig. 3H. Both PF127 hydrogel and ZnMet-PF127 presented a porous structure with similar pore size. The porous structure suggests the good breathability of ZnMet-PF127 which contributes to skin wound healing.

(**A**) Photograph of PF127. (**B-E**) Rheological behavior of ZnMet-PF127 at different concentrations. G′, elastic modulus; G″, viscous modulus. (**F**) Drug release of ZnMet-PF127. (**G**) Representative TEM images of PF127 hydrogels and ZnMet-PF127 hydrogels. Scale bar, 50 nm. (**H**) Representative SEM images of PF127 hydrogels and ZnMet-PF127 hydrogels. Scale bar, 50 μm.

Table 3
Proton positions and δ-chemical shift (ppm) of Met and ZnMet.

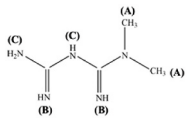

Met

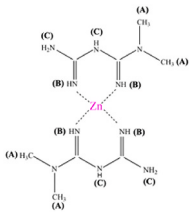

ZnMet

Position of protons	δ-Chemical shift (ppm) in Met	δ-Chemical shift (ppm) in ZnMet
A	2.91	2.91
B	7.22	7.19
	6.80	6.64
C	1.12	0.83

4.2. ZnMet greatly promotes cell proliferation and exerts potent antibacterial effect

The proliferation of fibroblast and endothelial cells are important for the recovery of the skin defect. Here, we examined the cell proliferation/toxicity and antibacterial effect of ZnMet. As shown in Fig. 4A, when ZnMet concentration was below 50 μM, there was a positive relationship between NIH3T3 proliferation and ZnMet concentration. However, when the concentration of ZnMet was over 50 μM, the proliferation rate of NIH3T3 decreased dose-dependently. There was a similar relationship between the proliferation rate of HUVEC and the concentration of ZnMet. The most suitable concentration of ZnMet for the proliferation of HUVEC was also around 50 μM (Fig. 4A). At the same time, we demonstrated that 50 μM ZnMet has a better effect on the proliferation rates of both NIH3T3 and HUVEC than Met or $ZnCl_2$ alone. Based on these results, we chose 50 μM of ZnMet as the working concentration in this study.

Inhibition of skin wound infection should be helpful for skin defect

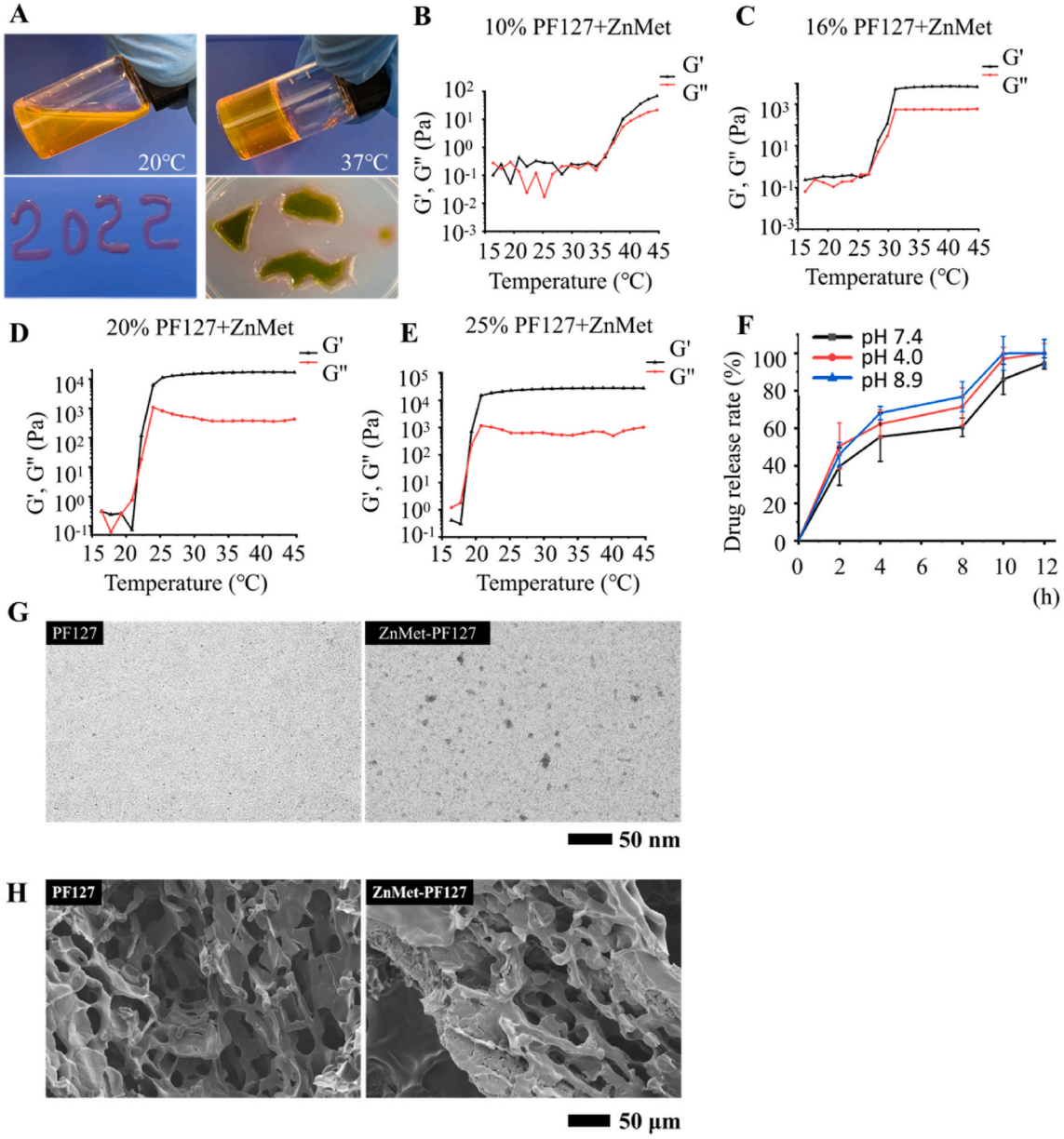

Fig. 3. Characterization of ZnMet-PF127.

recovery. In clinical, wound infections dramatically delay the recovery process of the wounds [66–68]. Here, we used gram-positive bacteria *S. aureus* and gram-negative bacteria *E. coli* to evaluate the antibacterial effect of ZnMet. As showed in Fig. 4B and C, bacteriostatic function of 50 μM ZnMet was similar to $ZnCl_2$ on *S. aureus*. Colony number in $ZnCl_2$ and ZnMet group was dramatically decreased compared with control or Met group. There were about 2.5×10^5 and 2.43×10^5 colonies in control group and Met group, respectively. This number was reduced to about 3100 in $ZnCl_2$ and 2966 in ZnMet group, respectively. In the case of *E. coli*, the antibacterial effect of ZnMet was the best among all the groups. Colony number of *E. coli* in control and Met group was similar, about 1.5×10^5 in the former and 1.25×10^5 in the latter. The colony number was significantly decreased in both $ZnCl_2$ group (3048 colonies) and ZnMet group (only 398 colonies) compared with control group. Collectively, for both bacteria, ZnMet exhibited the best antibacterial properties, indicating that the complexation of Zn ion to Met improves the bacteriostatic function of Zn ion [69]. Thus, these results suggest that ZnMet could lower the risk of wound infection during the process of skin wound healing.

(A) Cell proliferation assay of NIH3T3 and HUVEC using CCK8 kit. (**B** and **C**) Antibacterial assay of ZnMet (50 μM). *S. aureus* and *E. coli* were incubated with Met (100 μM), ZnMet (50 μM) and $ZnCl_2$ (50 μM) for 24 h. All results are displayed as mean ± SD. $^*p < 0.05$, $^{**}p < 0.01$ and $^{***}p < 0.001$, one-way ANOVA using the Tukey post-test. All experiments were performed with three replicates and independently repeated twice, qualitatively identical results were obtained.

4.3. ZnMet-PF127 drastically accelerates the healing of full-thickness skin defect

We examined the effect of ZnMet-PF127 on wound healing in vivo by employing the full-thickness skin defect model which is commonly used [70–72]. The modeling process and grouping information can be found in "Materials and Methods" part. The wounds were medicated every 24 h. Before each treatment, a thin layer of dry PF127 hydrogel left by the last treatment could be seen on the wound surface, which can effectively separate the wound from the external environment and reduce the occurrence of wound infection. As displayed in Fig. 5A, typical photos of

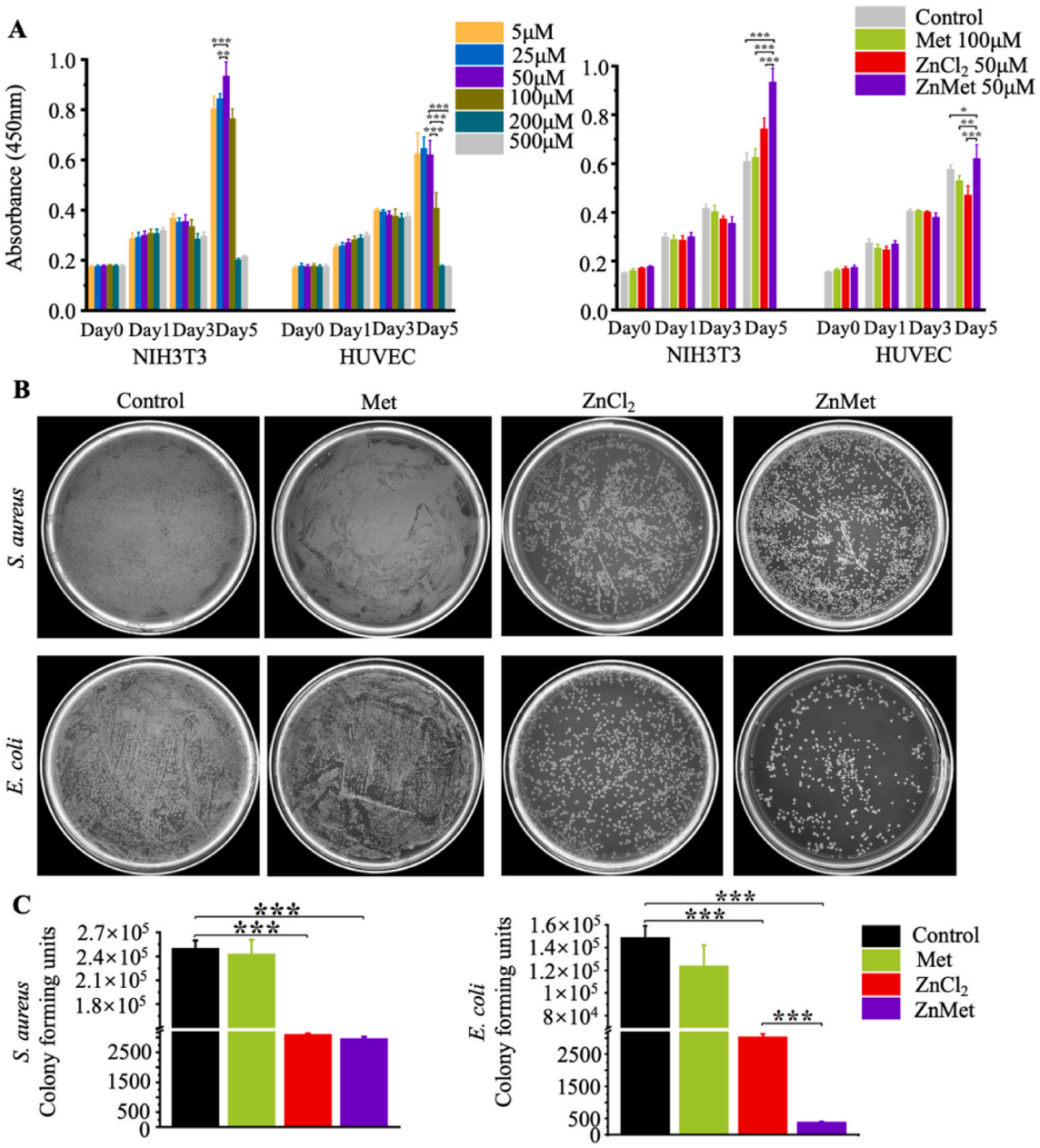

Fig. 4. ZnMet promotes NIH3T3 and HUVEC proliferation and inhibits growth of *S. aureus* and *E. coli*.

wounds at different time points showed that ZnMet-PF127 significantly accelerated the skin wound healing process compared with other groups. Most wounds healed completely at day 9 after surgery in ZnMet-PF127 group. Fig. 5B and C demonstrated that at all time points (day 1, 3, 5, 7, and 9), the healing rate of the wound in ZnMet-PF127 group was significantly faster than in other groups, especially after day 5.

(A) Representative photographs of wounds at day 1, 3, 5, 7 and 9. (**B**) Traces of wound-bed closure during 9 days for each treatment. Scale bar, 5 mm. (**C**) Wound contraction for each treatment. Scale bar, 5 mm. All results are displayed as mean ± SD. N = 6 mice per group. $*p < 0.05$, $**p < 0.01$ and $***p < 0.001$, (**C**) one-way ANOVA using the Tukey post-test.

4.4. ZnMet-PF127 significantly increases collagen deposition and new vessel formation

Depending on the healing of the skin wound, all mice were sacrificed at day 11 after surgery. At this point in time, viewed from outside the wound, the skin wounds of ZnMet-PF127-treated mice were almost closed. The skin defect area was removed and soaked in 4% formalin, dehydrated, and embedded in paraffin, then sectioned into 5 μm for histological analysis. H&E staining revealed that the wound width in ZnMet-PF127 group was the smallest among all groups (Fig. 6A). In ZnMet-PF127 group, the wound tissue has been switched from granulomatous phase to collagen formation phase, however, it was still in the granulomatous phase in other groups. Collagen deposition after granulation tissue formation is beneficial to wound healing. We observed larger amount collagen deposition in ZnMet-PF127 group compared with the other groups (Fig. 6B and F). Two-photon collagen images showed the most abundant and assembly collagen fibers in ZnMet-PF127 group (Fig. 6C and G). Masson staining also displayed the highest collagen-occupied area in ZnMet-PF127 group (Fig. 6B and F). These data suggest that ZnMet-PF127 helps healing of skin wound at least in part by increasing collagen deposition. The number of blood vessels reflects the quality of wound healing. CD31 immunohistochemical

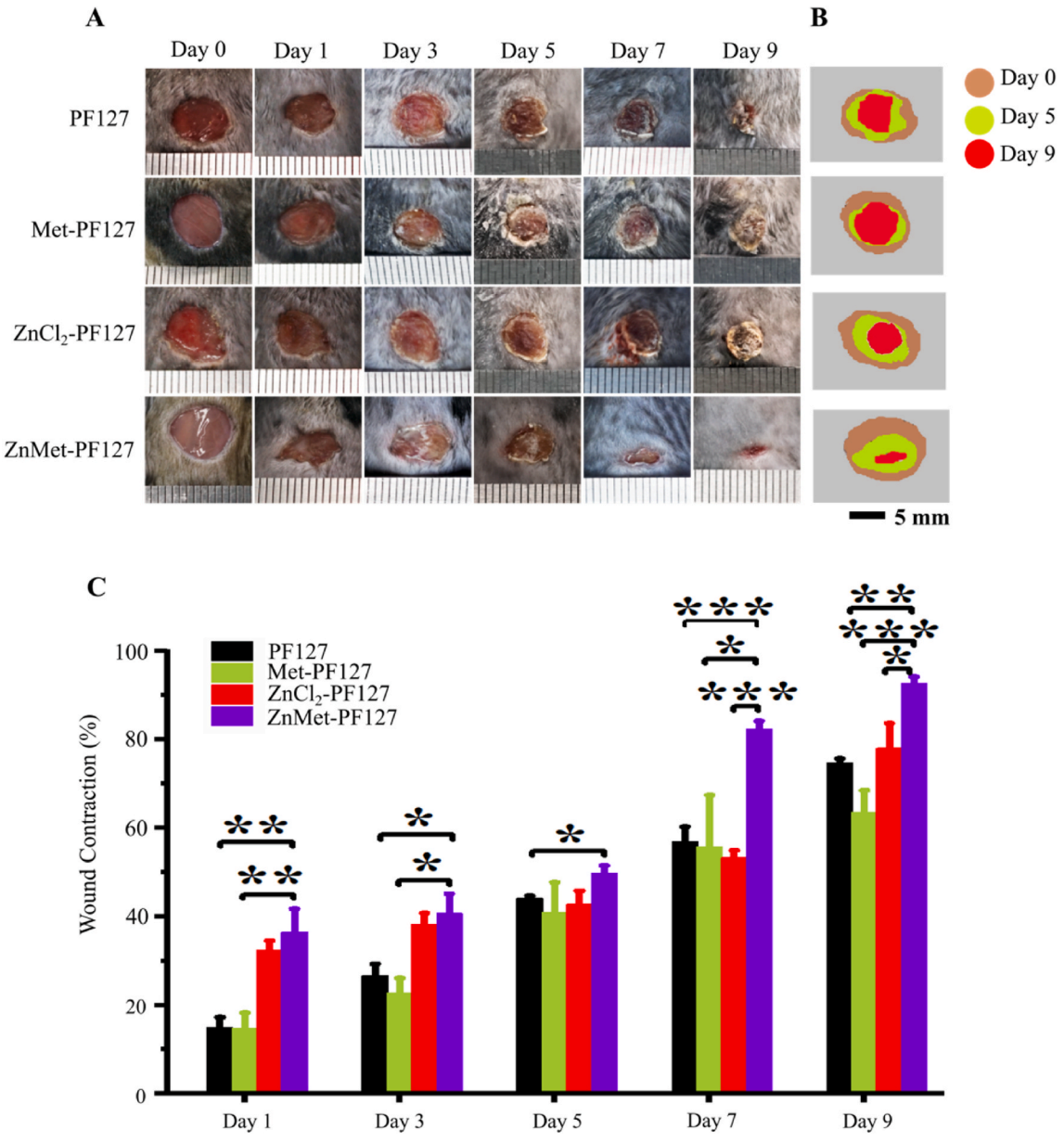

Fig. 5. ZnMet-PF127 enhances skin wound closure.

staining demonstrated that the density of new vessels in the wound site in ZnMet-PF127 group was the highest among all the groups (Fig. 6D and H), indicating that ZnMet-PF127 promotes wound healing partially through increasing new vessel formation.

H&E staining **(A)**, Masson trichrome staining **(B)** and two photon microscope images **(C)** of healed skin tissues at determined time. Scale bar, 100 μm. **(D)** Immunohistochemical staining of CD31. Scale bar, 30 μm. Quantitative analysis of wound length from H&E staining **(E)**, collagen occupied percentage from Masson trichrome staining **(F)** and fluorescence intensity from two photon microscope image **(G)**. Quantitative analysis of vessels **(H)**. All results are displayed as mean ± s.d. N = 6 mice per group. $*p < 0.05$, $**p < 0.01$ and $***p < 0.001$, one-way ANOVA using the Tukey post-test.

4.5. *ZnMet-PF127 exerts strong anti-inflammation and pro-angiogenesis effects during wound healing process*

Immunofluorescence staining of F4/80 and TNF-α suggested the potent anti-inflammatory effect of ZnMet-PF127 (Fig. 7A–D). The signal intensity of TNF-α in ZnMet-PF127 group was the weakest compared with other groups (Fig. 7A and B). Also, the relative coverage of F4/80 in ZnMet-PF127 group was the lowest among all groups (Fig. 7C and D). Moreover, RT-qPCR analysis displayed that the transcription of inflammatory relative genes such as *IL-1β, IL-6, TNF-α, iNOS* were drastically decreased and *VEGF* was increased in ZnMet treated NIH3T3 (Fig. 7E). Interestingly, we found that while the expression of TNF-α protein was the highest in $ZnCl_2$-PF127 group, the mRNA level was the highest in Met group (Fig. 7A and E). We repeated three times and obtained similar results. This inconsistency between in vitro and in vivo results may be due to different cell compositions. Skin tissue contains a variety of cell types. Although, the expression levels of TNF-α protein or mRNA were not so consistent in some groups between in vivo and in vitro experiments, both protein and mRNA level of TNF-α was the lowest in ZnMet-PF127 group. The increased *VEGF* expression partially explained why ZnMet could promote new vessel formation. Therefore, we demonstrated that ZnMet can facilitate skin wound healing through multi-biological functions. The above results suggest that ZnMet-PF127 facilitates skin wound healing at least partially by inhibition of

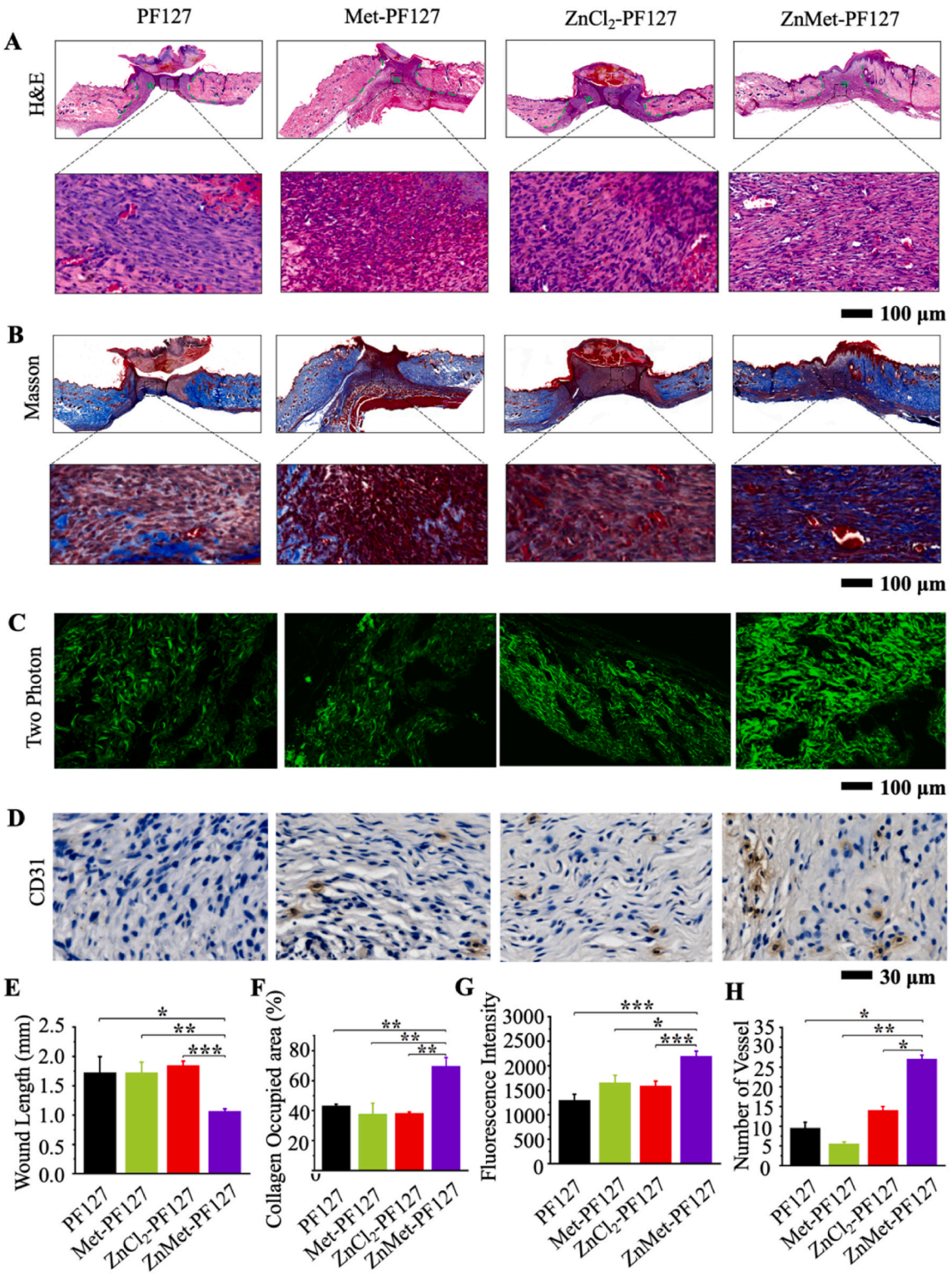

Fig. 6. ZnMet-PF127 greatly promotes granulation tissue formation, collagen deposition and new vessel formation.

inflammation and promoting new vessel formation. Researchers have reported that both $ZnCl_2$ and Met has inhibitory effect on inflammation [8,9,15,73]. In our study, the inflammation inhibitory effect of either $ZnCl_2$ or Met was not obvious, this discrepancy may be due to the low concentrations we used in this project. Previous studies have shown that the non-toxic concentration of Zn^{2+} to fibroblast and vascular endothelial cells ranges from 0 to 50 μM. Higher concentrations of Zn^{2+} could lead to proliferation inhibition or even cell death [74]. According to the clinical oral dose of Met, its blood concentration was 1–9 mg h L^{-1}. Our experimental concentration of Met was 0.7 mg h L^{-1}, much lower than the clinical blood concentration of Met [75–77]. However, despite the low concentration we used, ZnMet exhibited strong inhibitory effect on inflammation both in vivo and in vitro. This is of great clinical significance, the lower concentrations of drugs used, the less potential side effects could be caused.

Immunofluorescence staining of TNF-α **(A)**, F4/80 **(C)** and

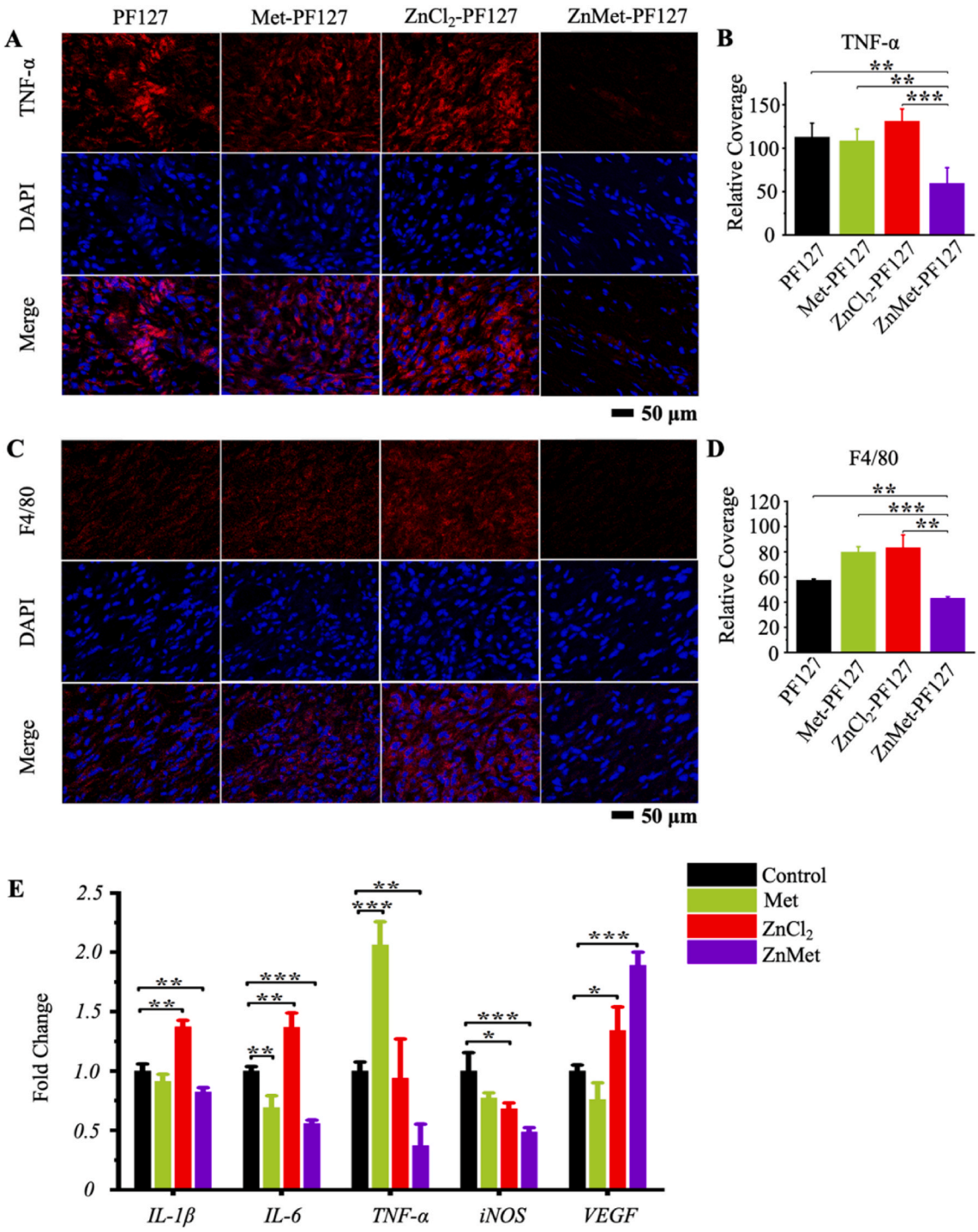

Fig. 7. ZnMet-PF127 has potent anti-inflammation and pro-angiogenesis effect.

quantitative analysis of immunofluorescence intensity **(B and D)**. Scale bar, 50 μm. All results are displayed as mean ± s.d. N = 6 mice per group. $*p < 0.05$, $**p < 0.01$ and $***p < 0.001$, versus controls, student's *t*-test. **(E)** Real-time qPCR (RT-qPCR) analysis of the effects of Met, ZnMet and $ZnCl_2$ on *IL-1β*, *IL-6*, *TNF-α*, *iNOS* and *VEGF* gene expression in NIH3T3 cells. $*p < 0.05$, $**p < 0.01$ and $***p < 0.001$, one-way ANOVA using the Tukey post-test.

4.6. ZnMet enhances autophagy and inhibits ROS production

Excessive accumulation of reactive oxygen species (ROS) can break cell homeostasis, leading to oxidative stress, increased production of inflammatory factors and mitochondrial dysfunction [78]. To study if ZnMet could inhibit inflammation and maintain cell homeostasis through inhibiting ROS production, we detected ROS in NIH3T3 with different treatment. As shown in Fig. 8A and C, ZnMet significantly inhibited ROS production compared with the other groups, suggesting that ZnMet could protect cells from oxidative stress induced damage by inhibiting ROS production.

Metformin can induce autophagy to reduce cell oxidative damage [79], probably through activating AMPK/mTOR/p70S6K pathway [80]. Here we detected autophagosome formed in NIH3T3 cells after treated

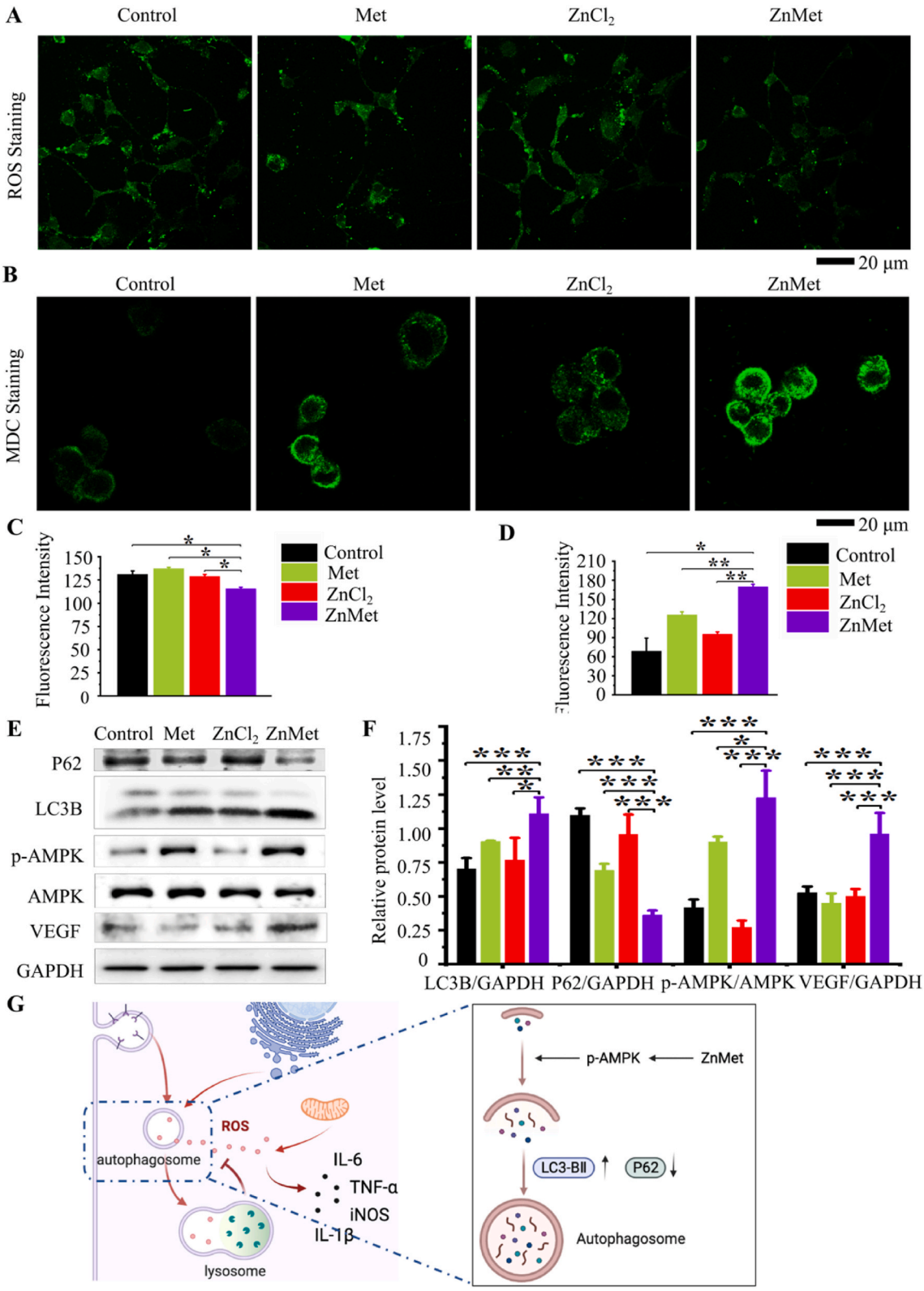

Fig. 8. ZnMet enhances autophagy and inhibits ROS production.

with ZnMet and other control drugs by MDC staining (Fig. 8B and D). Obviously, compared with blank control group, Met, $ZnCl_2$ and ZnMet all induced the formation of autophagosomes in NIH3T3 to varying degrees, and ZnMet induced the largest amount of autophagosomes. Western blot analysis showed in Fig. 8E and F indicated that compared with blank control, Met or $ZnCl_2$ group, autophagy related protein P62 was significantly reduced while autophagy protein LC3B was increased in ZnMet group, suggesting that ZnMet could promote autophagy in NIH3T3 cells. As expected, protein level of p-AMPK was significantly increased in ZnMet group. Furthermore, compared with blank control group, Met group and $ZnCl_2$ group, ZnMet strongly induced the expression of VEGF protein in NIH3T3, consistent with the increased

mRNA level (Fig. 7E), further demonstrating that ZnMet can promote angiogenesis. It has been well demonstrated that autophagy can promote angiogenesis by inducing the expression and secretion of VEGF [81–84]. Collectively, the above results demonstrated that ZnMet could promote skin wound healing by promoting cell autophagy, angiogenesis and inhibiting ROS production through activation of AMPK.

Immunofluorescence staining of ROS **(A)**, MDC Staining of autophagosome **(B)** and quantitative analysis of immunofluorescence intensity **(C and D)**. Scale bar, 20 μm. All results are displayed as mean ± s.d. N = 6 mice per group. $*p < 0.05$, $**p < 0.01$ and $***p < 0.001$, versus controls, Student's *t*-test. **(E)** Western blot analysis for the protein levels of P62, LC3B, p-AMPK, AMPK and VEGF in NIH3T3 cells and quantitative analysis of the protein levels of P62, LC3B, p-AMPK, AMPK and VEGF in NIH3T3 cells **(F)**. **(G)** Working model showing the anti-ROS mechanism of ZnMet in the treatment of skin wound. $*p < 0.05$, $**p < 0.01$ and $***p < 0.001$, one-way ANOVA using the Tukey post-test.

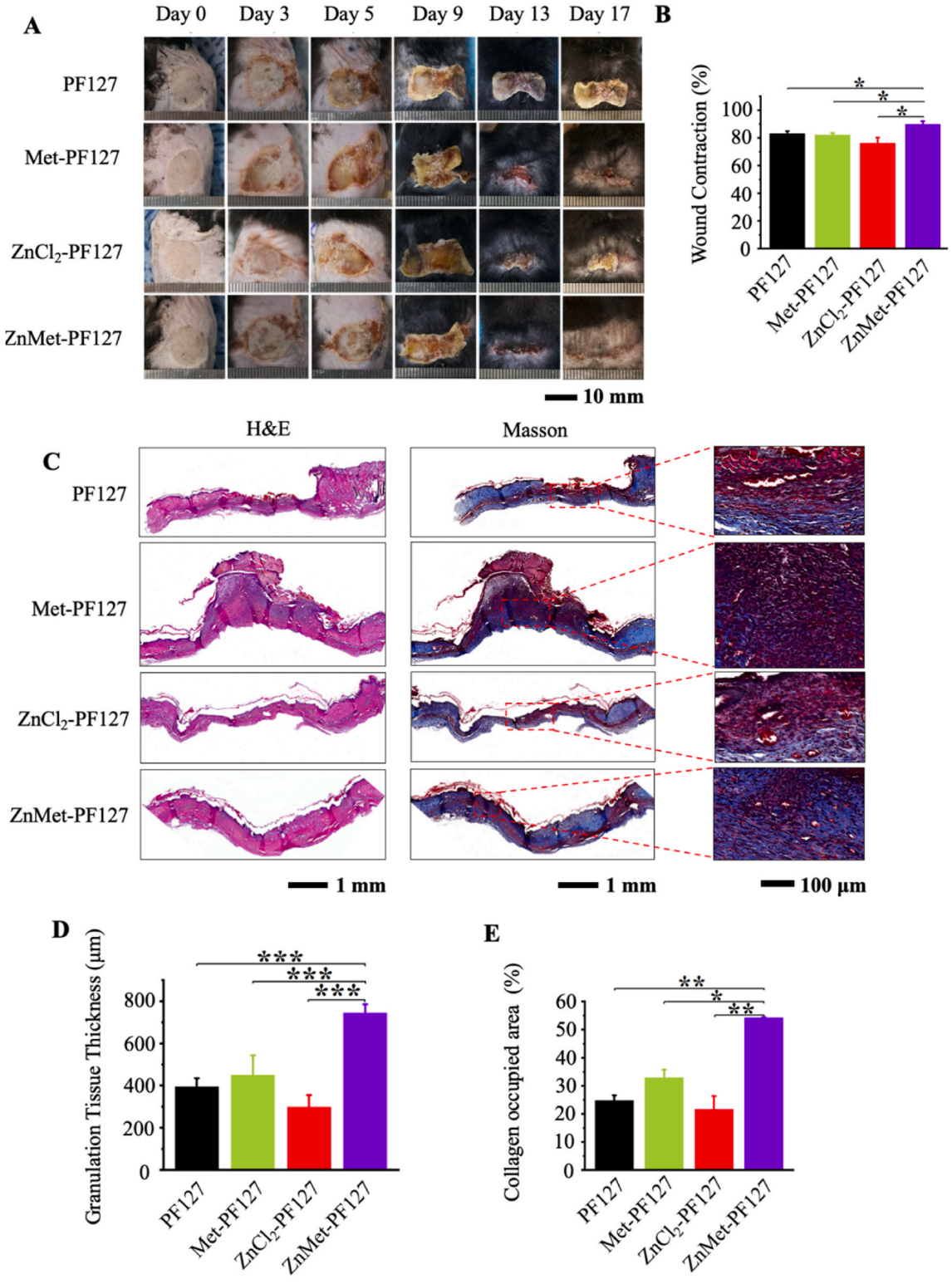

Fig. 9. ZnMet-PF127 greatly enhances the healing of burn skin injury.

4.7. ZnMet-PF127 dramatically accelerates wound healing of burn skin injury

Given that ZnMet-PF127 has potent antibacterial and anti-inflammatory properties, we also tested the effect of ZnMet-PF127 on the healing of burn skin injuries, which are notable by severe inflammation and a potential risk of infection [85–87]. We established mouse skin burn model as previously reported [49,50]. The modeling process and grouping information can be found in "Materials and Methods" part. Representative photos of skin wounds at different time points were shown in Fig. 9A. Obviously, the healing rate was fastest in ZnMet-PF127 group after 9 days, and the wounds in this group were almost completely closed at day 17 (Fig. 9B), thus all mice were sacrificed at day 17 after surgery.

H&E staining and Masson staining were used to analyze the histological changes. The scalded wound morphology was revealed by H&E staining in Fig. 9C. Completely healed wounds and thick granulation tissues could be seen in mice treated with ZnMet-PF127, while mice in groups treated with PF127, Met-PF127 or $ZnCl_2$-PF127 were characterized by less fully healed wounds and relative thin granulation tissues. Meanwhile, the scalded wound has been completely covered by epidermal layer, and the granulation tissue thickness was highest in ZnMet-PF127 group compared with other groups (Fig. 9D). Masson staining showed more collagen deposition in ZnMet-PF127 group than in other groups (Fig. 9C and E). Thus, the potent effect of ZnMet-PF127 on burn skin wound healing is also at least in part because it can efficiently promote the secretion and deposition of collagen fibers in the skin.

(**A**) Representative photographs of skin wounds at day 0, 3, 5, 9, 13 and 17. H&E staining, Masson trichrome staining (**B**) of skin tissues at wound sites at day 17. Quantitative analysis of the granulation tissue thickness (**E**) and collagen occupied area percentage (**F**) of the wounds at day 17. Scale bar, 10 mm, 1 mm and 100 μm. All results are displayed as mean ± SD. N = 6 mice per group. $^*p < 0.05$, $^{**}p < 0.01$ and $^{***}p < 0.001$, one-way ANOVA using the Tukey post-test.

4.8. The concentration of ZnMet used in this study has great biosafety

To study the biosafety of PF127, Met-PF127, $ZnCl_2$-PF127 and ZnMet-PF127 at specific concentrations used in our study in vivo, we examined the pathological changes of heart, liver, spleen, lung and kidney of mice by H&E staining. The results showed in Fig. 10 displayed that compared with PF127, Met-PF127, $ZnCl_2$-PF127 or ZnMet-PF127 treatment all has no toxic effect, all organs examined showed normal tissue and cell structure, indicating that the concentration of ZnMet used in this study have a reliable biosafety in mice.

Representative H&E staining photographs of heart, liver, spleen, lung and kidney of mice after treatment with PF127, Met-PF127, $ZnCl_2$-PF127 and ZnMet-PF127 at specific concentration. Scale bar, 200 μm. N = 6 mice per group.

5. Discussion and conclusion

In present study, we establish the potent role of ZnMet-PF127 in promoting skin wound healing, including traumatic skin wound and burn skin injury. ZnMet-PF127 greatly accelerates skin wound healing at least partially through promoting granulation tissue formation, collagen deposition, new vessel formation, and inhibiting ROS accumulation and inflammation.

Although the use of thermosensitive hydrogel in wound healing has been reported previously [88], here we for the first time use thermosensitive hydrogel PF127 as a spray by a nebulizer for skin wound healing. It acts as a therapeutic barrier, provide moisturization and relief pain, absorb extrudates, prevent bacterial infection. The porous structure of PF127 allows drug release evenly in tissues and serves as a delivery system for small molecules and drugs. In our study, 20% PF127 is

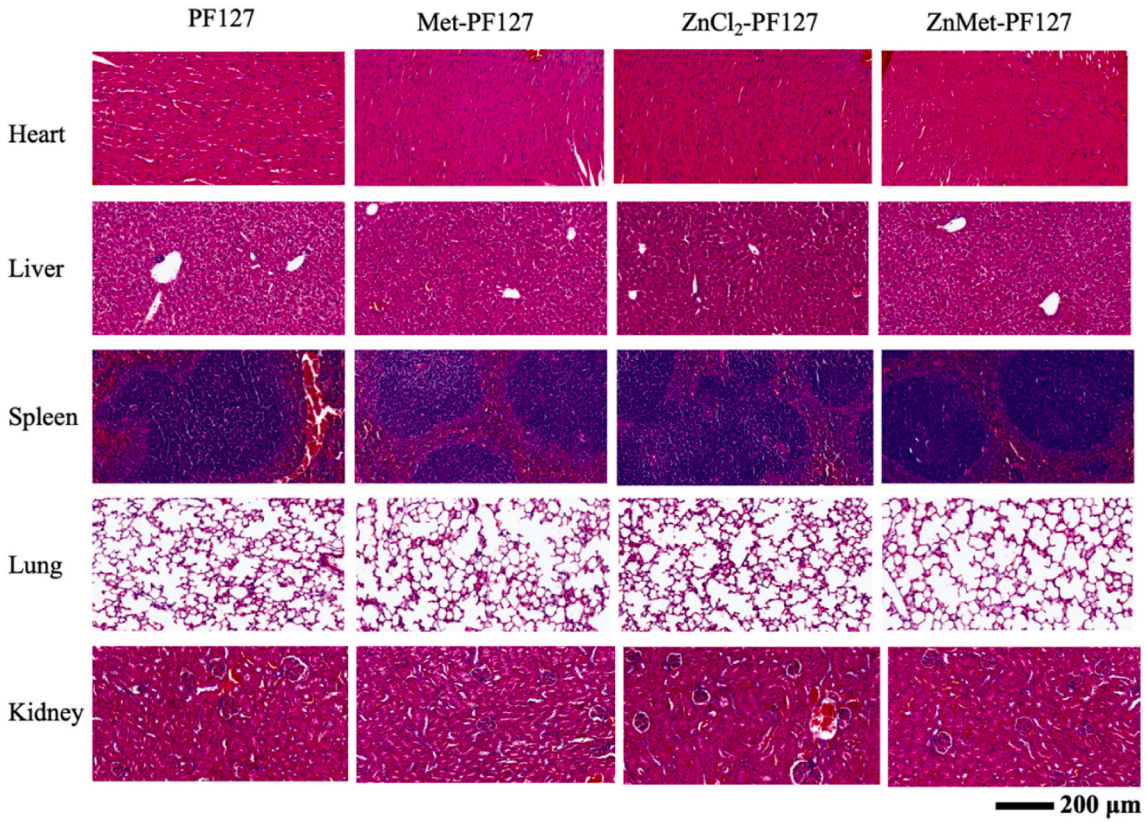

Fig. 10. ZnMet-PF127 at the concentration of 50 μM has no toxic effect on tissues and organs in vivo.

used as a scaffold to load ZnMet complexes. The load of ZnMet complexes to PF127 doesn't change the properties of PF127 demonstrated by examination of rheological behavior. Sprayable ZnMet-PF127 could fill in irregular skin defects evenly in a liquid state. After sprayed onto the skin, ZnMet-PF127 immediately switches from a liquid state to a semi-solid state and forms a shield between skin wound and external environment which reduces the incidence of wound infection.

In this study, we provide strong evidence that ZnMet-PF127 sprayable adhesive is a potentially effective drug for treatment of skin wounds, including traumatic skin wound and burn skin injury. First, the wound tissue in ZnMet-PF127 treated group has been switched from granulomatous phase to collagen formation phase while the other groups are still in the granulomatous phase. Second, there is more collagen formed in ZnMet-PF127 treated group than in other groups. Third, protein or mRNA expression levels of inflammation related genes, including *IL-1β, IL-6, TNF-α* and *iNOS,* are significantly decreased in ZnMet-PF127 treated group compared with other groups. Fourth, both the mRNA and protein level of VEGF and the vessel density in ZnMet-PF127 treated group in wound site are much higher than in other groups. More importantly, our data demonstrate that ZnMet could inhibit ROS production through activation of autophagy, probably by activating AMPK signal, thereby protecting cell from oxidative stress induced damage and promoting angiogenesis, thus contributing to increase the process of skin wound healing. We also demonstrate that ZnMet exhibits potent antibacterial effect on both *S. aureus* and *E. coli*, further reduces the risk of wound infection.

Common skin wounds and burn skin wounds are usually irregular in shape and depth and due to the severity and complexity of burn skin wounds, traditional sheet-like wound dressings are not always appropriate. Sprayable ZnMet-PF127 allows for easy, fast, and large-scale dressing changes.

Collectively, our study for the first time demonstrates the use of thermosensitive hydrogel PF127 as a spray by a nebulizer for skin wound healing, and for the first time we establish the potent effect of sprayable ZnMet-PF127 on the healing of traumatic skin wound and burn skin injury. We believe that ZnMet-PF127 is a potential clinical treatment for skin wound and has great economical and clinical value.

CRediT authorship contribution statement

Zhengwei Liu: Conceptualization, Data curation, Formal analysis, Investigation, Methodology, Resources, Software, Roles, Writing – original draft. **Wanze Tang:** Data curation, Formal analysis, Investigation. **Jiayi Liu:** Data curation, Formal analysis, Investigation. **Yingying Han:** Data curation, Investigation. **Qinnan Yan:** Data curation, Investigation. **Yuechao Dong:** Data curation, Investigation, Writing – review & editing. **Xiaomei Liu:** Data curation. **Dazhi Yang:** Data curation. **Guixing Ma:** Conceptualization, Data curation, Formal analysis, Investigation, Methodology, Project administration, Resources, Software, Supervision, Validation, Visualization, Roles, Writing – original draft, Writing – review & editing. **Huiling Cao:** Conceptualization, Data curation, Formal analysis, Funding acquisition, Project administration, Resources, Supervision, Validation, Visualization, Roles, Writing – original draft, Writing – review & editing.

Declaration of competing interest

HC, ZL, and GM filed a patent for the development of the ZnMet based spray for skin wound healing.

Acknowledgments

The authors acknowledge the assistance of Core Research Facilities of Southern University of Science and Technology. This work was supported, in part, by the National Key Research and Development Program of China Grants (2019YFA0906001), National Natural Science Foundation of China Grants (82022047 and 81972100), Guangdong Provincial Science and Technology Innovation Council Grant (2017B030301018).

Appendix A. Supplementary data

Supplementary data to this article can be found online at https://doi.org/10.1016/j.bioactmat.2022.06.008.

References

[1] J. Li, C. Zhou, C. Luo, B. Qian, S. Liu, Y. Zeng, J. Hou, B. Deng, Y. Sun, J. Yang, Q. Yuan, A. Zhong, J. Wang, J. Sun, Z. Wang, N-acetyl cysteine-loaded graphene oxide-collagen hybrid membrane for scarless wound healing, Theranostics 9 (2019) 5839–5853.

[2] D.W. Ferreira, C. Ulecia-Morón, P.A. Alvarado-Vázquez, K. Cunnane, C. Moracho-Vilriales, R.L. Grosick, T.M. Cunha, E.A. Romero-Sandoval, CD163 overexpression using a macrophage-directed gene therapy approach improves wound healing in ex vivo and in vivo human skin models, Immunobiology 225 (2020), 151862.

[3] Y. Xiao, J. Peng, Q. Liu, L. Chen, K. Shi, R. Han, Q. Yang, L. Zhong, R. Zha, Y. Qu, Z. Qian, Ultrasmall CuS@BSA nanoparticles with mild photothermal conversion synergistically induce MSCs-differentiated fibroblast and improve skin regeneration, Theranostics 10 (2020) 1500–1513.

[4] H.N. Suh, H.J. Han, Sonic hedgehog increases the skin wound-healing ability of mouse embryonic stem cells through the microRNA 200 family, Br. J. Pharmacol. 172 (2015) 815–828.

[5] H. Li, X. Han, K. Zuo, L. Li, J. Liu, X. Yuan, Y. Shen, M. Shao, D. Pang, Y. Chu, B. Zhao, miR-23b promotes cutaneous wound healing through inhibition of the inflammatory responses by targeting ASK1, Acta Biochim. Biophys. Sin. 50 (2018) 1104–1113.

[6] A.D. Kandhare, J. Alam, M.V. Patil, A. Sinha, S.L. Bodhankar, Wound healing potential of naringin ointment formulation via regulating the expression of inflammatory, apoptotic and growth mediators in experimental rats, Pharm. Biol. 54 (2016) 419–432.

[7] B. Khodr, Z. Khalil, Modulation of inflammation by reactive oxygen species: implications for aging and tissue repair, Free Radic. Biol. Med. 30 (2001) 1–8.

[8] A. Arbab, X. Lu, I.M. Abdalla, A.A. Idris, Z. Chen, M. Li, Y. Mao, T. Xu, Z. Yang, Metformin inhibits lipoteichoic acid-induced oxidative stress and inflammation through AMPK/NRF2/NF-κB signaling pathway in bovine mammary epithelial cells, Front. Vet. Sci. 8 (2021), 661380.

[9] W. Ba, Y. Xu, G. Yin, J. Yang, R. Wang, S. Chi, Y. Wang, C. Li, Metformin inhibits pro-inflammatory responses via targeting nuclear factor-κB in HaCaT cells, Cell Biochem. Funct. 37 (2019) 4–10.

[10] X. Xu, S. Lin, Y. Chen, X. Li, S. Ma, Y. Fu, C. Wei, C. Wang, W. Xu, The effect of metformin on the expression of GPR109A, NF-κB and IL-1β in peripheral blood leukocytes from patients with type 2 diabetes mellitus, Ann. Clin. Lab. Sci. 47 (2017) 556–562.

[11] H.J. Son, J. Lee, S.Y. Lee, E.K. Kim, M.J. Park, K.W. Kim, S.H. Park, M.L. Cho, Metformin attenuates experimental autoimmune arthritis through reciprocal regulation of Th17/Treg balance and osteoclastogenesis, Mediat. Inflamm. 2014 (2014), 973986.

[12] Y. Liu, G. Tang, Y. Li, Y. Wang, X. Chen, X. Gu, Z. Zhang, Y. Wang, G.Y. Yang, Metformin attenuates blood-brain barrier disruption in mice following middle cerebral artery occlusion, J. Neuroinflammation 11 (2014) 177.

[13] C. Bulcão, F.F. Ribeiro-Filho, A. Sañudo, F.S. Roberta, Effects of simvastatin and metformin on inflammation and insulin resistance in individuals with mild metabolic syndrome, Am. J. Cardiovasc. Drugs 7 (2007) 219–224.

[14] M. Gharib, W. Elbaz, E. Darweesh, N.A. Sabri, M.A. Shawki, Efficacy and safety of metformin use in rheumatoid arthritis: a randomized controlled study, Front. Pharmacol. 12 (2021), 726490.

[15] P. Dandona, A. Aljada, H. Ghanim, P. Mohanty, C. Tripathy, D. Hofmeyer, A. Chaudhuri, Increased plasma concentration of macrophage migration inhibitory factor (MIF) and MIF mRNA in mononuclear cells in the obese and the suppressive action of metformin, J. Clin. Endocrinol. Metab. 89 (2004) 5043–5047.

[16] Y. Ishibashi, T. Matsui, M. Takeuchi, S. Yamagishi, Metformin inhibits advanced glycation end products (AGEs)-induced renal tubular cell injury by suppressing reactive oxygen species generation via reducing receptor for AGEs (RAGE) expression, Horm. Metab. Res. 44 (2012) 891–895.

[17] J.E. Chang, M.S. Choi, A molecular perspective on the potential benefits of metformin for the treatment of inflammatory skin disorders, Int. J. Mol. Sci. 21 (2020).

[18] L. Qing, J. Fu, P. Wu, Z. Zhou, F. Yu, J. Tang, Metformin induces the M2 macrophage polarization to accelerate the wound healing via regulating AMPK/mTOR/NLRP3 inflammasome singling pathway, AM J. TRANSL RES. 11 (2019) 655–668.

[19] W. Li, W. Ma, H. Zhong, W. Liu, Q. Sun, Metformin inhibits proliferation of human keratinocytes through a mechanism associated with activation of the MAPK signaling pathway, Exp. Ther. Med. 7 (2014) 389–392.

[20] E. Goethe, K. Laarmann, J. Lührs, M. Jarek, J. Meens, A. Lewin, R. Goethe, Critical role of zur and SmtB in zinc homeostasis of Mycobacterium smegmatis, mSystems 5 (2020).

[21] C.M. Kibiti, A.J. Afolayan, Herbal therapy: a review of emerging pharmacological tools in the management of diabetes mellitus in Africa, PHARMACOGN MAG 11 (2015) S258–S274.
[22] U. Doboszewska, P. Wlaź, G. Nowak, K. Młyniec, Targeting zinc metalloenzymes in coronavirus disease 2019, Br. J. Pharmacol. 177 (2020) 4887–4898.
[23] M. Mehdipour, Z.A. Taghavi, K.I. Asvadi, A. Hosseinpour, A comparison between zinc sulfate and chlorhexidine gluconate mouthwashes in the prevention of chemotherapy-induced oral mucositis, Daru 19 (2011) 71–73.
[24] H.L. Hsieh, C.C. Lin, R.H. Shih, L.D. Hsiao, C.M. Yang, NADPH oxidase-mediated redox signal contributes to lipoteichoic acid-induced MMP-9 upregulation in brain astrocytes, J. Neuroinflammation 9 (2012) 110.
[25] J. Li, X. Liu, L. Tan, Z. Cui, X. Yang, Y. Liang, Z. Li, S. Zhu, Y. Zheng, K. Yeung, X. Wang, S. Wu, Zinc-doped Prussian blue enhances photothermal clearance of Staphylococcus aureus and promotes tissue repair in infected wounds, Nat. Commun. 10 (2019) 4490.
[26] R. Olar, M. Badea, D. Marinescu, M.C. Chifiriuc, C. Bleotu, M.N. Grecu, E. E. Iorgulescu, V.N. Lazar, N-dimethylbiguanide complexes displaying low cytotoxicity as potential large spectrum antimicrobial agents, Eur. J. Med. Chem. 45 (2010) 3027–3034.
[27] H. Cheng, Z. Shi, K. Yue, X. Huang, Y. Xu, C. Gao, Z. Yao, Y.S. Zhang, J. Wang, Sprayable hydrogel dressing accelerates wound healing with combined reactive oxygen species-scavenging and antibacterial abilities, Acta Biomater. 124 (2021) 219–232.
[28] S. Jacob, A.B. Nair, J. Shah, N. Sreeharsha, S. Gupta, P. Shinu, Emerging role of hydrogels in drug delivery systems, tissue engineering and wound management, Pharmaceutics 13 (2021).
[29] H.F. Salem, Sustained-release progesterone nanosuspension following intramuscular injection in ovariectomized rats, Int. J. Nanomed. 5 (2010) 943–954.
[30] E.R. Shearier, P.K. Bowen, W. He, A. Drelich, J. Drelich, J. Goldman, F. Zhao, In vitro cytotoxicity, adhesion, and proliferation of human vascular cells exposed to zinc, ACS Biomater. Sci. Eng. 2 (2016) 634–642.
[31] F.B. Ma, N. Liu, N. Hu, C.Y. Wen, B. Tang, Synthesis of strontium chondroitin sulfate and the evaluation of its capability to attenuate osteoarthritis, Carbohydr. Polym. 170 (2017) 217–225.
[32] D. Guo, Nashunchaoketu, J. Wang, X. Liu, S. Wu, X. Zhao, B. Yang, [Simultaneous determination of four highly polar anti-diabetic drugs in Chinese traditional patent medicines using high performance liquid chromatography], Se Pu 27 (2009) 211–215.
[33] S. Chatterjee, P.C. Hui, E. Wat, C.W. Kan, P.C. Leung, W. Wang, Drug delivery system of dual-responsive PF127 hydrogel with polysaccharide-based nano-conjugate for textile-based transdermal therapy, Carbohydr. Polym. 236 (2020), 116074.
[34] F. Tirnaksiz, J.R. Robinson, Rheological, mucoadhesive and release properties of pluronic F-127 gel and pluronic F-127/polycarbophil mixed gel systems, Pharmazie 60 (2005) 518–523.
[35] S.L. Da, A.C. Borges, M.G. de Oliveira, M.A. de Farias, Visualization of supramolecular structure of Pluronic F127 micellar hydrogels using cryo-TEM, MethodsX 7 (2020), 101084.
[36] J. Qu, X. Zhao, Y. Liang, T. Zhang, P.X. Ma, B. Guo, Antibacterial adhesive injectable hydrogels with rapid self-healing, extensibility and compressibility as wound dressing for joints skin wound healing, Biomaterials 183 (2018) 185–199.
[37] B. Guo, C. Tang, M. Wang, Z. Zhao, H.A. Shokoohi-Tabrizi, B. Shi, O. Andrukhov, X. Rausch-Fan, In vitro biocompatibility of biohybrid polymers membrane evaluated in human gingival fibroblasts, J. Biomed. Mater. Res. B Appl. Biomater. 108 (2020) 2590–2598.
[38] G. Wu, F. Ma, Y. Xue, Y. Peng, L. Hu, X. Kang, Q. Sun, D.F. Ouyang, B. Tang, L. Lin, Chondroitin sulfate zinc with antibacterial properties and anti-inflammatory effects for skin wound healing, Carbohydr. Polym. 278 (2022), 118996.
[39] H. Cao, K. Zhu, L. Qiu, S. Li, H. Niu, M. Hao, S. Yang, Z. Zhao, Y. Lai, J.L. Anderson, J. Fan, H.J. Im, D. Chen, G.D. Roodman, G. Xiao, Critical role of AKT protein in myeloma-induced osteoclast formation and osteolysis, J. Biol. Chem. 288 (2013) 30399–30410.
[40] H. Cao, Q. Yan, D. Wang, Y. Lai, B. Zhou, Q. Zhang, W. Jin, S. Lin, Y. Lei, L. Ma, Y. Guo, Y. Wang, Y. Wang, X. Bai, C. Liu, J.Q. Feng, C. Wu, D. Chen, X. Cao, G. Xiao, Focal adhesion protein Kindlin-2 regulates bone homeostasis in mice, BONE RES 8 (2020) 2.
[41] I. Tedesco, R.G. Luigi, F. Nazzaro, M. Russo, R. Palumbo, Antioxidant effect of red wine anthocyanins in normal and catalase-inactive human erythrocytes, J. Nutr. Biochem. 12 (2001) 505–511.
[42] Y. Liu, L. Chen, Q. Gong, H. Jiang, Y. Huang, Hypoxia-induced mitophagy regulates proliferation, migration and odontoblastic differentiation of human dental pulp cells through FUN14 domain-containing 1, Int. J. Mol. Med. 49 (2022).
[43] Y. Lei, X. Fu, P. Li, S. Lin, Q. Yan, Y. Lai, X. Liu, Y. Wang, X. Bai, C. Liu, D. Chen, X. Zou, X. Cao, H. Cao, G. Xiao, LIM domain proteins Pinch1/2 regulate chondrogenesis and bone mass in mice, BONE RES 8 (2020) 37.
[44] X. Fu, B. Zhou, Q. Yan, C. Tao, L. Qin, X. Wu, S. Lin, S. Chen, Y. Lai, X. Zou, Z. Shao, M. Wang, D. Chen, W. Jin, Y. Song, H. Cao, G. Zhang, G. Xiao, Kindlin-2 regulates skeletal homeostasis by modulating PTH1R in mice, Signal Transduct. Targeted Ther. 5 (2020) 297.
[45] J. Wu, N.X. Landén, Investigation of skin wound healing using a mouse model, Methods Mol. Biol. 2154 (2020) 239–247.
[46] J. Yoon, J.H. Park, J.W. Choi, Y.C. Kim, Optimal fluence and duration of low-level laser therapy for efficient wound healing in mice, Ann. Dermatol. 33 (2021) 318–323.
[47] J.W. Hong, W.J. Lee, S.B. Hahn, B.J. Kim, D.H. Lew, The effect of human placenta extract in a wound healing model, Ann. Plast. Surg. 65 (2010) 96–100.
[48] S. Balaji, M. LeSaint, S.S. Bhattacharya, C. Moles, Y. Dhamija, M. Kidd, L.D. Le, A. King, A. Shaaban, T.M. Crombleholme, P. Bollyky, S.G. Keswani, Adenoviral-mediated gene transfer of insulin-like growth factor 1 enhances wound healing and induces angiogenesis, J. Surg. Res. 190 (2014) 367–377.
[49] P. Ren, D.W. Guan, R. Zhao, W.X. Ma, S.T. Zhang, [Establishment of skin scald model in mice], Fa Yi Xue Za Zhi 28 (2012) 92–94, 99.
[50] S. Kim, J. Kwon, Thymosin beta 4 improves dermal burn wound healing via downregulation of receptor of advanced glycation end products in db/db mice, Biochim. Biophys. Acta 1840 (2014) 3452–3459.
[51] D. Abdel-Gawad, W.A. Moselhy, R.R. Ahmed, H.M. Al-Muzafar, K.A. Amin, M. M. Amin, E.S. El-Nahass, K. Abdou, Therapeutic effect of mesenchymal stem cells on histopathological, immunohistochemical, and molecular analysis in second-grade burn model, Stem Cell Res. Ther. 12 (2021) 308.
[52] A. Khan, H. Bai, A. Khan, Z. Bai, Neferine prevents ultraviolet radiation-induced skin photoaging, Exp. Ther. Med. 19 (2020) 3189–3196.
[53] K. Zhu, H. Jiao, S. Li, H. Cao, D.L. Galson, Z. Zhao, X. Zhao, Y. Lai, J. Fan, H.J. Im, D. Chen, G. Xiao, ATF4 promotes bone angiogenesis by increasing VEGF expression and release in the bone environment, J. Bone Miner. Res. 28 (2013) 1870–1884.
[54] M. Lombardo, M. Parekh, S. Serrao, A. Ruzza, S. Ferrari, G. Lombardo, Two-photon optical microscopy imaging of endothelial keratoplasty grafts, Graefes Arch. Clin. Exp. Ophthalmol. 255 (2017) 575–582.
[55] X. Jiang, J. Zhong, Y. Liu, H. Yu, S. Zhuo, J. Chen, Two-photon fluorescence and second-harmonic generation imaging of collagen in human tissue based on multiphoton microscopy, Scanning 33 (2011) 53–56.
[56] M.S. Refat, F.M. Al-Azab, H.M. Al-Maydama, R.R. Amin, Y.M. Jamil, M.I. Kobeasy, Synthesis, spectroscopic and antimicrobial studies of La(III), Ce(III), Sm(III) and Y (III) Metformin HCl chelates, Spectrochim. Acta Mol. Biomol. Spectrosc. 142 (2015) 392–404.
[57] F.A. Al-Saif, M.S. Refat, Synthesis, spectroscopic, and thermal investigation of transition and non-transition complexes of metformin as potential insulin-mimetic agents, J. Therm. Anal. Calorim. 111 (2013) 2079–2096.
[58] P. Hiwale, S. Lampis, G. Conti, C. Caddeo, S. Murgia, A.M. Fadda, M. Monduzzi, In vitro release of lysozyme from gelatin microspheres: effect of cross-linking agents and thermoreversible gel as suspending medium, Biomacromolecules 12 (2011) 3186–3193.
[59] S.G. Choi, S.E. Lee, B.S. Kang, C.L. Ng, E. Davaa, J.S. Park, Thermosensitive and mucoadhesive sol-gel composites of paclitaxel/dimethyl-β-cyclodextrin for buccal delivery, PLoS One 9 (2014), e109090.
[60] G. Grassi, A. Crevatin, R. Farra, G. Guarnieri, A. Pascotto, B. Rehimers, R. Lapasin, M. Grassi, Rheological properties of aqueous Pluronic-alginate systems containing liposomes, J. Colloid Interface Sci. 301 (2006) 282–290.
[61] E. Ibrahim, S. Ismail, G. Fetih, O. Shaaban, K. Hassanein, N.H. Abdellah, Development and characterization of thermosensitive pluronic-based metronidazole in situ gelling formulations for vaginal application, Acta Pharm. 62 (2012) 59–70.
[62] A. Shawesh, S. Kallioinen, O. Antikainen, J. Yliruusi, Influence of storage time and temperature on the stability of indomethacin Pluronic F-127 gels, Pharmazie 57 (2002) 690–694.
[63] M.A. Attia, I. El-Gibaly, S.E. Shaltout, G.N. Fetih, Transbuccal permeation, anti-inflammatory activity and clinical efficacy of piroxicam formulated in different gels, Int. J. Pharm. 276 (2004) 11–28.
[64] T. Cui, J. Yu, C.F. Wang, S. Chen, Q. Li, K. Guo, R. Qing, G. Wang, J. Ren, Micro-gel ensembles for accelerated healing of chronic wound via pH regulation, Adv. Sci. (2022), e2201254.
[65] K. Derakhshandeh, M. Fashi, S. Seifoleslami, Thermosensitive Pluronic hydrogel: prolonged injectable formulation for drug abuse, Drug Des. Dev. Ther. 4 (2010) 255–262.
[66] P.G. Hogan, R.L. Mork, R.M. Thompson, C.E. Muenks, M.G. Boyle, M.L. Sullivan, J. J. Morelli, C.V. Williams, N. Sanchez, D.A. Hunstad, J.B. Wardenburg, S.J. Gehlert, C.D. Burnham, A. Rzhetsky, S.A. Fritz, Environmental methicillin-resistant Staphylococcus aureus contamination, persistent colonization, and subsequent skin and soft tissue infection, JAMA Pediatr. 174 (2020) 552–562.
[67] S. Das, J. Li, J. Iaconis, D. Zhou, G.G. Stone, J.L. Yan, D. Melnick, Ceftaroline fosamil doses and breakpoints for Staphylococcus aureus in complicated skin and soft tissue infections, J. Antimicrob. Chemother. 74 (2019) 425–431.
[68] S. Das, J. Li, J. Iaconis, D. Zhou, G.G. Stone, J.L. Yan, D. Melnick, Ceftaroline fosamil doses and breakpoints for Staphylococcus aureus in complicated skin and soft tissue infections, J. Antimicrob. Chemother. 74 (2019) 425–431.
[69] C. Ning, X. Wang, L. Li, Y. Zhu, M. Li, P. Yu, L. Zhou, Z. Zhou, J. Chen, G. Tan, Y. Zhang, Y. Wang, C. Mao, Concentration ranges of antibacterial cations for showing the highest antibacterial efficacy but the least cytotoxicity against mammalian cells: implications for a new antibacterial mechanism, Chem. Res. Toxicol. 28 (2015) 1815–1822.
[70] L. Rhea, M. Dunnwald, Murine excisional wound healing model and histological morphometric wound analysis, JoVE (162) (2020).
[71] X. Xiong, J. Liang, Y. Xu, J. Liu, Y. Liu, The wound healing effects of the Tilapia collagen peptide mixture TY001 in streptozotocin diabetic mice, J. Sci. Food Agric. 100 (2020) 2848–2858.
[72] S. Balaji, M. LeSaint, S.S. Bhattacharya, C. Moles, Y. Dhamija, M. Kidd, L.D. Le, A. King, A. Shaaban, T.M. Crombleholme, P. Bollyky, S.G. Keswani, Adenoviral-mediated gene transfer of insulin-like growth factor 1 enhances wound healing and induces angiogenesis, J. Surg. Res. 190 (2014) 367–377.
[73] A.S. Prasad, B. Bao, F.W. Beck, O. Kucuk, F.H. Sarkar, Antioxidant effect of zinc in humans, Free Radic. Biol. Med. 37 (2004) 1182–1190.

[74] E.R. Shearier, P.K. Bowen, W. He, A. Drelich, J. Drelich, J. Goldman, F. Zhao, In vitro cytotoxicity, adhesion, and proliferation of human vascular cells exposed to zinc, ACS Biomater. Sci. Eng. 2 (2016) 634–642.
[75] R.N. Qu, W. Qu, Metformin inhibits LPS-induced inflammatory response in VSMCs by regulating TLR4 and PPAR-γ, Eur. Rev. Med. Pharmacol. Sci. 23 (2019) 4988–4995.
[76] S. Yari, H.H. Khoei, M. Saber, F. Esfandiari, A. Moini, M. Shahhoseini, Metformin attenuates expression of angiogenic and inflammatory genes in human endometriotic stromal cells, Exp. Cell Res. 404 (2021), 112659.
[77] Y. Han, F. Yuan, C. Deng, F. He, Y. Zhang, H. Shen, Z. Chen, L. Qian, Metformin decreases LPS-induced inflammatory response in rabbit annulus fibrosus stem/progenitor cells by blocking HMGB1 release, Aging (Albany NY) 11 (2019) 10252–10265.
[78] L. Li, J. Tan, Y. Miao, P. Lei, Q. Zhang, ROS and autophagy: interactions and molecular regulatory mechanisms, Cell. Mol. Neurobiol. 35 (2015) 615–621.
[79] M. De Santi, G. Baldelli, A. Diotallevi, L. Galluzzi, G.F. Schiavano, G. Brandi, Metformin prevents cell tumorigenesis through autophagy-related cell death, Sci. Rep. 9 (2019) 66.
[80] X. Guo, M. Liang, Metformin alleviates dexamethasone-induced apoptosis by regulating autophagy via AMPK/mTOR/p70S6K in osteoblasts, Exp. Cell Res. 415 (2022), 113120.
[81] Y. Li, X. Zhao, B. He, W. Wu, H. Zhang, X. Yang, W. Cheng, Autophagy activation by hypoxia regulates angiogenesis and apoptosis in oxidized low-density lipoprotein-induced preeclampsia, Front. Mol. Biosci. 8 (2021), 709751.
[82] J.H. Lu, Y.H. Wu, T.J. Juan, H.Y. Lin, R.J. Lin, K.S. Chueh, Y.C. Lee, C.Y. Chang, Y. S. Juan, Autophagy alters bladder angiogenesis and improves bladder hyperactivity in the pathogenesis of ketamine-induced cystitis in a rat model, Biology 10 (2021).
[83] R. Li, J.H. Du, G.M. Yao, Y. Yao, J. Zhang, Autophagy: a new mechanism for regulating VEGF and PEDF expression in retinal pigment epithelium cells, Int. J. Ophthalmol. 12 (2019) 557–562.
[84] J. Yin, G. Gong, C. Sun, Z. Yin, C. Zhu, B. Wang, Q. Hu, Y. Zhu, X. Liu, Angiopoietin 2 promotes angiogenesis in tissue-engineered bone and improves repair of bone defects by inducing autophagy, Biomed. Pharmacother. 105 (2018) 932–939.
[85] M. Liang, Z. Chen, F. Wang, L. Liu, R. Wei, M. Zhang, Preparation of self-regulating/anti-adhesive hydrogels and their ability to promote healing in burn wounds, J. Biomed. Mater. Res. B Appl. Biomater. 107 (2019) 1471–1482.
[86] J. Zhu, F. Li, X. Wang, J. Yu, D. Wu, Hyaluronic acid and polyethylene glycol hybrid hydrogel encapsulating nanogel with hemostasis and sustainable antibacterial property for wound healing, ACS Appl. Mater. Interfaces 10 (2018) 13304–13316.
[87] V. Gribova, F. Boulmedais, A. Dupret-Bories, C. Calligaro, B. Senger, N.E. Vrana, P. Lavalle, Polyanionic hydrogels as reservoirs for polycationic antibiotic substitutes providing prolonged antibacterial activity, ACS Appl. Mater. Interfaces 12 (2020) 19258–19267.
[88] D.Y. Zhu, Z.P. Chen, Z.P. Hong, L. Zhang, X. Liang, Y. Li, X. Duan, H. Luo, J. Peng, J. Guo, Injectable thermo-sensitive and wide-crack self-healing hydrogel loaded with antibacterial anti-inflammatory dipotassium glycyrrhizate for full-thickness skin wound repair, Acta Biomater. 143 (2022) 203–215.